



TÉCNICO
LISBOA

Application of Similitude Laws for The Design of Electromechanical Models Using High-Temperature Superconductors

Pedro Rafael Rebelo Gonçalves da Rocha

Thesis to obtain the Master of Science Degree in

Electrical and Computer Engineering

Supervisor(s): Prof. Paulo José da Costa Branco
MSc. Francisco Ferreira da Silva

Examination Committee

Chairperson: Prof. Célia Maria Santos Cardoso de Jesus

Supervisor: Prof. Paulo José da Costa Branco

Member of the Committee: Prof. Vitor Manuel de Oliveira Maló Machado

January 2021

Declaration

I declare that this document is an original work of my own authorship and that it fulfills all the requirements of the Code of Conduct and Good Practices of the Universidade de Lisboa

To my family, for the unconditional support.

Acknowledgments

First of all, I would like to thank Prof. Paulo Branco and especially to MSc. Francisco da Silva for their supports and constant help during the realization of this dissertation. I would like to thank also to all my colleagues in the Electrical Machine Laboratory for the advises and help. Finally, I would like to thank all my family and friends to all the support given during my academical path.

Resumo

A utilização de materiais supercondutores em máquinas elétricas é um tema que tem adquirido considerável relevância durante os últimos anos, permitindo projetar e conceber máquinas com maior eficiência e densidade de potência que as convencionais. No entanto, devido à complexidade destes materiais quando comparados com os materiais magnéticos convencionais, é necessário a realização de um estudo preliminar e qualitativo de modo a comparar as diferentes topologias.

O propósito desta dissertação passa por realizar um estudo comparativo entre máquinas convencionais e máquinas com supercondutores de altas temperaturas (HTS), usando para esse efeito o conceito de leis de escala. Primeiramente, será apresentado a aplicação das leis de escala em máquinas elétricas com ímãs permanentes (PM). De seguida, serão introduzidos os HTS, tais como as respetivas perdas, sendo este estudo realizado através de um modelo analítico simplificado, modelo de KIM. Será feito ainda um estudo comparativo entre máquinas convencionais e máquinas com HTS a substituírem PM ou os tradicionais enrolamentos de cobre. Finalmente, estudos experimentais e simulações foram realizados de modo a quantificar e validar as perdas encontradas nos blocos HTS, mais especificamente no YBCO.

Conclui-se, através das leis de escala, que as máquinas com HTS apresentam maior eficiência e densidade de potência, no entanto, novas topologias devem ser consideradas, especialmente para a situação em que os HTS substituem os PM. Tanto os estudos experimentais como as simulações realizadas em software de elementos finitos (FEM) revelaram-se inconclusivas, reforçando a necessidade da realização de experiências com um maior grau de precisão e complexidade.

Palavras-chave: Leis de Escala, Supercondutores de Alta Temperatura (HTS), YBCO, Perdas por Histerese

Abstract

The use of superconducting materials for implementation on electric machines is nowadays a relevant subject of research, for the design of new, more efficient, and power dense machines. Based on the physical behaviours of superconductors being more complex than conventional magnetic materials present in electric machines, preliminary and qualitative studies are necessary to compare the new potential superconducting electrical machines to conventional ones.

The aim of this dissertation is, then, to make a comparative study of both types of machines, using similitude laws, also called scale laws. This dissertation presents the study of similitude laws for high temperature superconductors (HTS) inserted in electric machines. First, scale laws are presented for the case of electric machines with permanent magnets. Then, HTS are introduced, as well as the scale laws representative of their losses regarding current density, magnetic flux density and volume. This study was made using a simplified analytical model, the Kim model. Second, the comparison between conventional machines and machines using HTS, being as permanent magnets, or as coils was performed. Third, experimental tests were performed, to quantify and validate the losses in YBCO bulks, also with additional validation on FEM simulations.

It was found by scale laws that HTS electric machines are indicative of having higher efficiencies and more power dense, however, the machine's topologies need to be different, especially using HTS as permanent magnets. The experimentations were inconclusive, as well as the FEM simulations, which indicates that a more precise and complex experiments need to be performed.

Keywords: Similitude Laws, High Temperature Superconductors (HTS), YBCO, Hysteresis Losses

Contents

- Acknowledgments v
- Resumo vii
- Abstract ix
- List of Tables xiii
- List of Figures xv
- Nomenclature xix
- Glossary 1

- 1 Introduction 1**
- 1.1 Motivation 2
- 1.2 Objectives 2
- 1.3 Thesis Outline 2

- 2 Similitude Laws 5**
- 2.1 Introduction 6
- 2.2 Characteristic length 6
- 2.3 Nominal Power 7
- 2.4 Power Losses and Efficiency 8
- 2.4.1 Joule Losses 8
- 2.4.2 Iron Losses 9
- 2.4.3 Efficiency 10
- 2.4.4 Temperature Dependence 11
- 2.5 Modular Configuration 12
- 2.5.1 Joule Losses 13
- 2.5.2 Temperature Dependence 14

- 3 High Temperature Superconductors 17**
- 3.1 Introduction 18
- 3.2 Maxwell's equations 18
- 3.3 E-J Power Law for HTS 19
- 3.4 Critical Region and Superconductor Type 22
- 3.5 Meissner effect and flux pinning 24

3.6	Joule Losses	25
3.7	KIM Electromagnetic Model	28
3.7.1	Introduction	28
3.7.2	Implementation	32
3.8	Hysteresis Losses	34
3.8.1	Introduction	34
3.8.2	Implementation Examples	35
4	Similitude Laws for YBCO	41
4.1	Magnetic density flux constant	42
4.1.1	Singular Configuration	42
4.1.2	Modular Configuration	44
4.1.3	Machine with YBCO as PM	46
4.2	Current density constant	47
4.2.1	Singular Configuration	47
4.2.2	Modular Configuration	49
4.2.3	Machine with YBCO as coils	50
5	Experimental and FEM simulations	51
5.1	Losses in YBCO - Experimentation	52
5.1.1	Experimental losses in a standard magnetic circuit	52
5.1.2	Experimental losses in a YBCO bulk as in a magnetic circuit	55
5.1.3	Iron Core Solution	59
5.2	FEM Model - Introduction	63
5.3	FEM - Geometric Description of the System	64
5.3.1	Iron Core and Coil	64
5.3.2	Iron Core, Coil and YBCO	65
5.4	FEM - Electromagnetic Model	66
5.4.1	A Formulation	66
5.4.2	Jiles Atherton Model	67
5.5	FEM - 3D Model for Iron and Coil	69
5.5.1	3D Simulation	69
5.5.2	Power losses	72
5.6	FEM - 3D Model for Iron, Coil and YBCO	73
5.6.1	3D Simulation	73
6	Conclusions	75
6.1	Achievements	75
6.2	Future Work	75
	Bibliography	77

List of Tables

3.1	Parameter values for YBCO [14]	26
3.2	Wall Temperature increase for different situations	27
5.1	Power and losses at air temperature for circuit iron + coil with air-gap	60
5.2	Power and losses for cooled circuit iron + coil with air-gap	61
5.3	Power and losses for cooled circuit iron + coil+ YBCO	61
5.4	Jiles-Atherton iron parameters	68
5.5	RMS voltage and current and power factor for simulated model iron + coil	72
5.6	Power and losses for simulated model iron + coil	72

List of Figures

2.1	Efficiency η as a relation of the linear dimension l . The efficiency is only considering joule losses.	9
2.2	Comparison between total efficiency and efficiency only considering joule losses with the increase of linear dimension, l	10
2.3	Logarithmic relation between power available with increase of l , considering temperature constraints or not.	12
2.4	Modular and singular ratio for power and volume	13
2.5	Relation between total module efficiency η_{mT} and the number of modules n	14
2.6	Relation between total module efficiency η_{mT} and the number of modules n	15
2.7	Relation between total module efficiency η_{mT} and the number of modules n	16
3.1	Dependency of the electric field with relative current density and m parameter at a logarithmic scale.	19
3.2	Critical current density and maximum critical current ratio in function of applied magnetic flux density for different values of B_0	20
3.3	Critical current density and maximum critical current ratio in function of applied magnetic flux density for different values of B_0	20
3.4	Critical temperature dependency with magnetic flux density	21
3.5	3D graph defining superconductive region [3].	22
3.6	Magnetization of a type I superconductor [10]	23
3.7	Magnetisation of a type II superconductor [10]	23
3.8	Example of meissner effect [3]	24
3.9	Example of Flux Pinning [11]	24
3.10	Resistivity in a logarithmic scale in function of Temperature	25
3.11	Superconductor bulk representation	28
3.12	Schematic representations of KIM model current and magnetic field behaviour	29
3.13	Schematic representations of KIM model current and magnetic field behaviour	30
3.14	Bulk penetration in function of the internal magnetic field	31
3.15	Figure from Matlab code for M-H analytic curve	32
3.16	M-H curve for external magnetic field amplitude's lower than H_p	33
3.17	M-H curve for external magnetic field amplitude's higher than H_p	33

3.18	Generic M-H curve for YBCO, scaled by H_p , for $H_m \leq H_p$.	34
3.19	M(H) curves for different radius and for $H_m=H_p$	35
3.20	M(B) curves with nominal values for $H_m=H_p$	36
3.21	Normalized (logarithmic) curve for W_h and M_{max} in function of radius for $H_m = H_p$	36
3.22	3D plot for radius, ratio of penetration and hysteresis losses	37
3.23	M(B) curve for different ratio of penetration with $r=0.02m$	38
3.24	Hysteresis density losses at a cycle for different ratio of penetration (logarithmic scale) with $r=0.02m$	38
3.25	M(H) for different temperatures with $r=0.02m$	39
4.1	Acquired data for hysteresis losses in function of volume and the best curve fitting for the situation with magnetic flux constant	42
4.2	Efficiency comparison between YBCO and joule losses in conductors.	43
4.3	Modular efficiency in function of number of modules	44
4.4	Comparison between the joule losses with temperature constraints and the hysteresis losses for YBCO in function of the number of modules	45
4.5	Efficiency for machine with PM and with YBCO	46
4.6	Acquired data for hysteresis losses in function of volume and the best curve fitting for the situation with current density constant	47
4.7	Efficiency comparison between YBCO and joule losses in conductors for density current constant	48
4.8	Modular efficiency in function of number of modules	49
4.9	Efficiency of a conventional PM machine, a machine with YBCO as PM and a machine with YBCO as coils with increase of linear dimension.	50
5.1	Simple Magnetic Circuit [13]	52
5.2	Typical B(H) anhysteretic curve	53
5.3	Example of Saturation Current [16]	54
5.4	Experimental circuit and data	54
5.5	Experimental 2 coils of 400 turns each	55
5.6	Illustration of experimental set up	55
5.7	Experimental current (blue) in amperes and voltage (red) in volts YBCO bulk as in a magnetic circuit	56
5.8	Experimental applied magnetic field for YBCO bulk as in a magnetic circuit	56
5.9	Experimental set up for coil with 4000 turns	57
5.10	Illustration of experimental set up for coil with 4000 turns	57
5.11	Experimental oscilloscope data	58
5.12	Experimental magnetic iron core circuit	59
5.13	Experimental magnetic iron core circuit with YBCO	60
5.14	Conceptual design of circuit iron + coil	63

5.15 Conceptual design of circuit iron + coil +YBCO	64
5.16 Front view of system iron + coil	64
5.17 Top view of system iron + coil	65
5.18 Front view of system iron + coil + YBCO	65
5.19 YBCO	66
5.20 Experimental and simulated B(H) curves	68
5.21 Magnetic flux density norm and streamlines results for an isometric view	69
5.22 Magnetic flux density norm and streamlines results for a side view	70
5.23 Experimental and simulated B(H) curve	70
5.24 Current at green and voltage at blue compute through FEM software	71
5.25 Current and voltage acquired experimentally	71
5.26 Magnetic flux density norm results for a side view for a Iron, Coil and YBCO system	73
5.27 Current, at blue, and voltage, at green, compute through FEM software for a Iron, Coil and YBCO system	74

Nomenclature

Greek symbols

$\alpha(T_0)$	Temperature coefficient
α, δ	Jiles-Atherton parameters
χ	Magnetic susceptibility
$\Delta\theta$	Thermal variation
ϵ_0	Electrical permeability of free space
η	Efficiency
μ	Magnetic permeability
μ_0	Magnetic permeability of free space
ω	Angular frequency
Φ	Magnetic flux
ϕ	Phase angle
ψ	Magnetic flux linkage
ρ	Electrical resistivity
ρ_q	Total charge density
σ	Electrical conductivity

Roman symbols

A	Magnetic potential vector
B	Magnetic flux density vector
D	Displacement vector field
E	Electric field vector
H	Electric field vector

\mathbf{J}	Current density vector
\mathbf{M}	Magnetization vector
A	Area
A	Surface area
a, c, k	Jiles-Atherton parameters
A_e	Surface area
B_0	E-J HTS Parameter
B_C	Critical magnetic flux density
B_{C1}	Lower critical magnetic field density.
B_{C2}	Higher critical magnetic field density.
E_0	E-J HTS Parameter
F	Magnetomotive force
h	Thermal transfer coefficient
H_0	KIM model parameters
H_C	Critical magnetic field
h_e	Conduction coefficient
H_p	Value of applied field for which the bulk is full with induced currents
I	Current
J_C	Critical current
J_{C0}	Maximum critical current
$J_{C0\beta}$	Critical current density at 0 K with no applied field
k_1	KIM model parameters
l	Characteristic length
l_c	Mean path
m	E-J HTS Parameter
M_{an}	Anhysteretic magnetization
M_{irr}	Irreversible magnetization
M_{max}	Maximum value of magnetization

m_p	Number of phases
M_s	Magnetization saturation
N	Turns
n	number of modules
p	Number of poles pairs
P_E	Eddy current's losses
P_H	Hysteresis losses
P_H	Hysteresis power density losses
P_J	Joule losses
P_m	Modular power
P_N	Nominal power
P_T	Total losses
q_G	Joule losses per volume.
R	DC resistance
r_0	Cylinder radius
RMS	Root Mean Square
T	Temperature
t	Time
T_C	Critical temperature
T_{C0}	Critical temperature when $B = 0$
T_{out}	Temperature that surrounds the cylinder walls
T_W	Temperature at cylinder walls
U	Voltage
V	Volume
W_H	Hysteresis density losses
X_L	Inductor reactance

Subscripts

PM Relative to Permanent Magnets

YBCO Relative to the YBCO

Superscripts

Cu Relative to Copper

FEM Relative to Finite Element Method

iron Relative to iron

PM Relative to Permanent Magnets

YBCO Relative to the YBCO

Chapter 1

Introduction

This chapter describes how this dissertation is structured. A brief topic overview of electromechanical superconductor machines and similitude laws in conventional machines is also presented. To conclude, the objectives and thesis outline are stated.

1.1 Motivation

Superconducting electromechanical machines have been researched since the 1950s for applications where higher efficiency and power density is required, however only with the discovery of the high temperature superconductors (HTS) in 1986, there was a major development in electric power applications. At this time were created the first HTS synchronous machines where an HTS field excitation winding can provide high magnetic flux density in the air gap with major reductions of excitation losses, this type of performance was unachievable with traditional field excitation systems, like copper coils or permanent magnets (PM). A PM motor rated at 7 MW for marine pod propulsor weighs about 120 tonnes, when an HTS synchronous motor concept would drastically reduce the weight of a podded electromechanical drive by 50% [1].

Another approach is the design of a synchronous reluctance machine with HTS bulk in the rotor. In synchronous reluctance machines, the rotor moves towards a position favouring a value of maximum magnetic flux. The torque produced by these machines is proportional to the difference between the stator inductance maximum value, L_{max} , and the minimum value L_{min} . It is possible to amplify this difference by using bulk HTS blocks on the rotor. The diamagnetic properties of superconductors make them ideal, leading to an increase of the L_{max} , which results in an increase of torque. In the last years had been a development in HTS machine solutions for industrial applications, the first HTS industrial motor rated at 1.2 MW was built by Rockwell Automation, and for energy production, like the 4MVA HTS generator developed by Siemens [2][3].

Another relevant subject is similitude (or scaling) laws. They are used to predict the performance of a new design based on data from an existing, similar design. In the electromagnetics, new design and similar design will have a similar geometry, but in general not the same materials and electromagnetic excitation [4]. This subject is very used in synchronous permanent magnet machines built to offshore wind turbines to maximized the relation available power and occupied volume (or weight) and for reducing the operational costs [5]. It is also used in switched reluctance motors (SRM) [6].

1.2 Objectives

The objectives of this thesis are: to study the losses and efficiency in an HTS (more precisely YBCO) and develop an experimental or simulated model that validates that; to study the losses and efficiency of YBCO when subject to similitude laws; to compare the losses and efficiency between a conventional machine and a machine with YBCO when subject both to similitude laws.

1.3 Thesis Outline

This thesis is divided into six chapters. Chapter 1 is an introductory one. Chapter 2 is dedicated to explaining and give some background in similitude laws. Chapter 3 is dedicated to give some background in HTS and to implement the KIM electromagnetic model for hysteresis losses estimation. Chapter 4

describes the application of similitude laws in YBCO and the comparison between them and conventional machines. Chapter 5 presents the experimental and simulation models. Chapter 6 completes this work presenting the main conclusions of this work.

Chapter 2

Similitude Laws

This chapter provides some background in dimensional analysis of generic electrical machines with permanent magnets and understand how the losses and consequently efficiency changes by increasing or decreasing the machine's size. This analysis comprises in seeing how the size of one machine influences the overall coil current density and the air gap magnetic flux density, as also as the implications of maintaining either the current density or the magnetic flux density constant. With the study of dimensional analysis, a modular configuration is considered, meaning the study of several smaller machines linked together mechanically, being the total combined mechanical power equal to a singular larger machine.

2.1 Introduction

One of the most important characteristic in electrical machines sizing is the relation between power available and occupied volume. The maximization of this relationship allows the decreasing of operational costs in facilities where electrical machines have a preponderant role.

Another important factor in operational costs regarding electrical machines is the pieces degradation, that leads to a partial or sometimes total replace of the machine, with increase the costs. One solution is the utilization of machines with modular configuration, this enables an easier replacement of the damage pieces, reducing the operational costs due to maintenance [5].

Therefore, the focus of this chapter will be understand how the machine efficiency can be maximized with the increase of size and with the use of a modular configuration.

2.2 Characteristic length

A very important concept in similitude laws is the concept of characteristic length, l , which represents one spacial dimension. To better understand this concept, consider a simple geometric body, like a parallelepiped. Dimensionally speaking, its volume, V , and its surface area, A , have a proportional relation with the characteristic length, l , that goes by,

$$V \propto l^3 \tag{2.1}$$

and

$$A \propto l^2 \tag{2.2}$$

The focus in this analysis is not to find the strict relationship between the variables, but the dimensional relationship between them, hence being proportional and not equal. With these characteristics, a first preliminary study can be made, to verify qualitatively what are the best approaches for the design of electric machines, regarding their efficiency.

2.3 Nominal Power

To understand what kind of proportionality the machine's efficiency has with its volume, is necessary to compute the nominal power of a generic electrical machine with PM. The nominal power of a machine can be stated as,

$$P_N \propto m_p p UI \propto UI \quad (2.3)$$

where U is the voltage, I is the current, m_p is the number of phases and p is the number of pole pairs.

If the voltage drop in the windings is negligible, the equation that defines the voltage in one phase of the machine can be approximated to,

$$U \approx \frac{d\psi}{dt} \quad (2.4)$$

where ψ represents the linked magnetic flux through each phase. In order to simplify the formulation of scale laws, the steady-state regime will be used, only considering the fundamental component, making the voltage U

$$U \approx \omega_F \psi \quad (2.5)$$

where ω_F is the angular electrical frequency in the stator poles.

In integral terms, Φ and I can be expressed as,

$$\Phi = \int_S (\mathbf{B} \cdot \mathbf{n}_s) dS \quad (2.6)$$

$$I = \int_S (\mathbf{J} \cdot \mathbf{n}_s) dS \quad (2.7)$$

where (2.6) and (2.7) are considered fluxes, which are dependent on a surface through each the vector field passes (in this case, the vector field are the \mathbf{B} and \mathbf{J}). Using the proportional relations between area and l , Φ and I can be expressed by

$$\Phi \propto Bl^2 \quad (2.8)$$

$$I \propto Jl^2 \quad (2.9)$$

Concluding, (2.3) with (2.5), (2.8) and (2.9) can be established as

$$P_N \propto \omega_F B J l^4 \propto l^4 \quad (2.10)$$

If it is considered that, for a given electric machine, the number of phases, number of pole pairs, the electric frequency, the magnetic flux density and the current density are kept constant, the nominal power will be then proportional to the characteristic length raised to 4, $P_N \propto l^4$ [5].

2.4 Power Losses and Efficiency

The relationships between the machine's size and efficiency are closely related to the machine's losses. In this sense, the relationships for the joule losses and iron losses need to be established.

2.4.1 Joule Losses

The joule losses in PM machines are due to the current that flows through the copper conductors. The volumetric density of power losses by the Joule's effect, P_J , is given by,

$$P_J = \int_V \mathbf{E} \cdot \mathbf{J} dV \quad (2.11)$$

where \mathbf{E} is the electric field vector, \mathbf{J} is the current density vector and V is the volume. Knowing that for a conductor $\mathbf{E} = \rho\mathbf{J}$, the (2.11) becomes

$$P_J = \int \rho \mathbf{J}^2 dV \quad (2.12)$$

Thus, using (2.12) for the proportional relation, P_J is

$$P_J \propto J^2 l^3 \propto l^3 \quad (2.13)$$

assuming that the resistivity and current density are constant values.

If the joule losses are the only one considered, the efficiency is written as

$$\eta_J = \frac{1}{1 + \frac{P_J}{P_N}} \quad (2.14)$$

where

$$\frac{P_J}{P_N} \propto \frac{m_p J^2 l^3}{m_p p \omega_F B J l^4} \propto \frac{J}{B l} \propto \frac{1}{l} \quad (2.15)$$

considering J and B constants.

To consider a machine with $\eta = 91\%$ when the linear dimension is normalized, $l = 1$, it is necessary to transform (2.14) in (2.16)

$$\eta_J = \frac{1}{1 + \frac{K_1}{l}} \quad (2.16)$$

where $K_1 = 0.099$.

Figure 2.1 shows the evolution of the efficiency η as the linear dimension l of the machine increases.

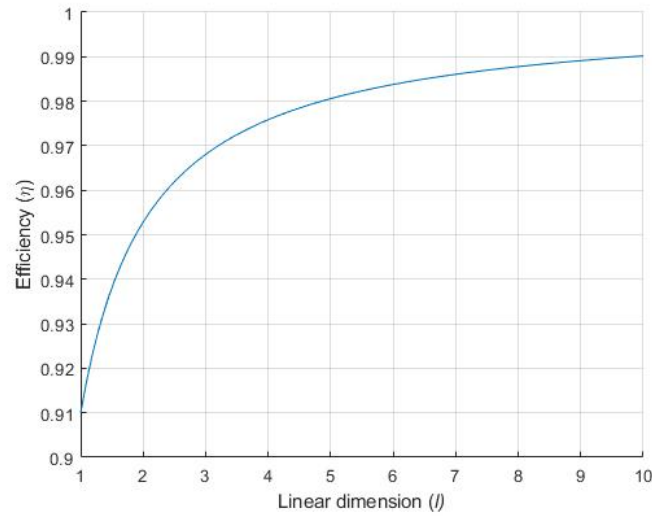


Figure 2.1: Efficiency η as a relation of the linear dimension l . The efficiency is only considering joule losses.

It is clear that, as the machine increases its size, the efficiency increases, with its limits at 100% of efficiency.

2.4.2 Iron Losses

The iron losses are divided in hysteresis losses and in losses due to eddy currents. The first ones are based on Steinmetz empirical relation given by

$$P_H \propto B^\alpha l^3 \quad (2.17)$$

where α depends on the material used. If B is considered constant the relation (2.17) becomes

$$P_H \propto l^3 \quad (2.18)$$

The losses due to eddy currents are given by the relation

$$P_E \propto B^2 l^3 \quad (2.19)$$

if B is considered constant the relation (2.19) becomes

$$P_E \propto l^3 \quad (2.20)$$

It is possible to conclude that iron losses and joule losses have the same proportional relation with the linear dimension [6]. In further analyses, the variable chosen will be the joule losses however, that deductions are equally valid for iron losses.

2.4.3 Efficiency

The total efficiency is defined by equation (2.21),

$$\eta_T = \frac{1}{1 + \frac{P_T}{P_N}} \quad (2.21)$$

where P_T represents the total power losses. The total power losses in the model is given by equation (2.22).

$$P_T = P_J + P_H + P_E \quad (2.22)$$

Considering (2.13),(2.18) and (2.20), the (2.22) becomes

$$P_T \propto 3l^3 \quad (2.23)$$

and the equation (2.21) becomes

$$\eta_T = \frac{1}{1 + \frac{3K_1}{l}} \quad (2.24)$$

Figure 2.2 shows the comparison between total efficiency and efficiency only considering joule losses with the increase of linear dimension.

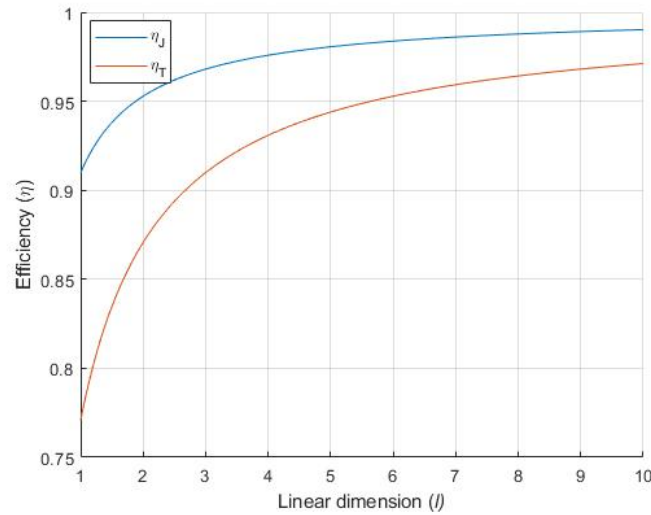


Figure 2.2: Comparison between total efficiency and efficiency only considering joule losses with the increase of linear dimension, l .

It can be seen that when all losses are considered, the efficiency when the linear dimension is normalized, $l = 1$, is smaller than when only joule losses are considered. However, it is possible to conclude that when the linear dimension increases, this difference become smaller, meaning that with the increase of sizing, considering the total losses or only joule losses will have the same practical effect.

2.4.4 Temperature Dependence

Another variable that needs to be controlled is the temperature elevation, this have extreme importance, since it dictates the continuous point of operation of the machine, as well as its operation lifetime.

It is considered that the thermal inertia in a magnetic material is higher than in a conductor, therefore the joule losses are the only relevant losses considered for this analysis. This means that the thermal variation, $\Delta\theta$, is proportional to the joule losses dissipated in an area through convection, as shown in (2.25),

$$\Delta\theta \propto \frac{P_J}{h_e A_e} \propto \frac{mJ^2 l^3}{l^2} \propto J^2 l \quad (2.25)$$

where h_e is the equivalent conduction coefficient for all heat exchanges, and A_e , the cooling equivalent surface area [5]. To control the temperature elevation, it is necessary to keep the thermal variation constant ($\Delta\theta = cte$)

$$\Delta\theta \propto J_\theta^2 l_\theta = J^2 l = cte \quad (2.26)$$

$$J = \frac{\sqrt{l_\theta}}{\sqrt{l}} J_\theta \quad (2.27)$$

with J_θ and l_θ the current density and linear dimension with temperature constraints, respectively.

The nominal power when the temperature constraint are considered is given by (2.28)

$$P_\theta \propto \omega_F B J l^4 \propto \omega_F B J_\theta \sqrt{l_\theta} l^{3,5} \propto l^{3,5} \quad (2.28)$$

Figure 2.3 shows the comparison between the power available when the temperature constraint are considered or not, with the increase of the linear dimension.

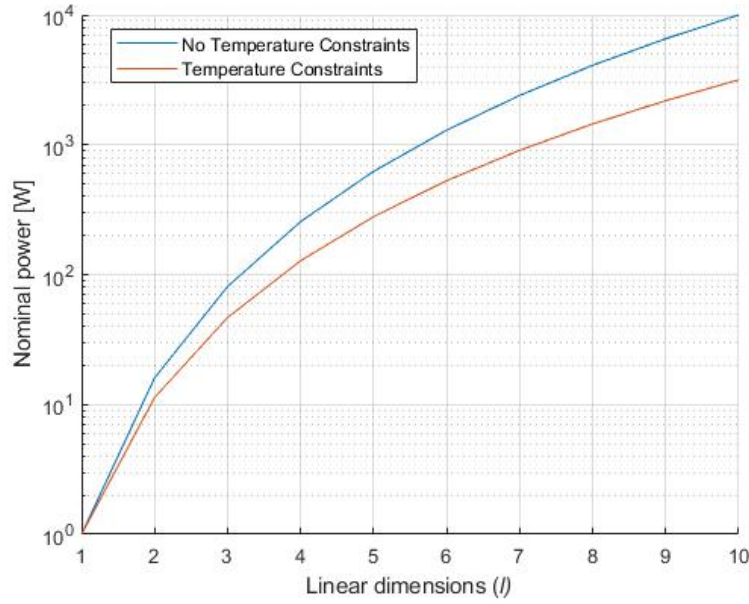


Figure 2.3: Logarithmic relation between power available with increase of l , considering temperature constraints or not.

It can be seen that the difference between the power considering temperature constraints or not is negligible for small linear dimension increases but relevant for bigger ones.

2.5 Modular Configuration

Another approach for a drive system is to have a modular configuration, i.e., multiple machines mechanically connected to achieve the same mechanical power and torque.

In this way, the modular power, P_m , i.e., the power that corresponds to one of the modules, can be expressed as

$$P_m = \frac{P}{n} \quad (2.29)$$

where n represent the number of modules and P represents the total power of the original drive system with only one machine.

Assuming B and J as constants and that the cubic linear dimension represents the volume of a geometry,

$$n = \frac{P}{P_m} = \frac{l^4}{l_m^4} \quad (2.30)$$

$$\frac{V_m}{V} = \left(\frac{l_m}{l}\right)^3 = \frac{1}{(\sqrt[4]{n})^3} \quad (2.31)$$

equation (2.31) relates the ratio between the volume of the module, V_m , and the volume of a single

machine configuration, V , with the number of modules [5].

Figure 2.4 shows the comparison between $\frac{V_m}{V}$ and $\frac{P_m}{P}$ for an increase in the number of modules.

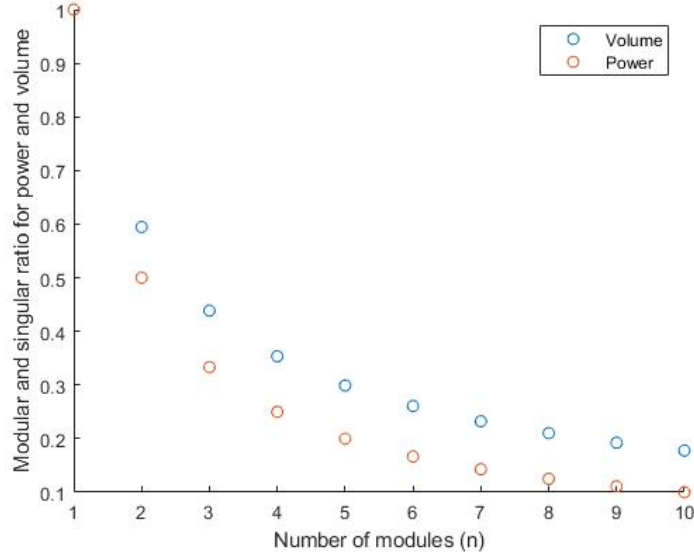


Figure 2.4: Modular and singular ratio for power and volume

Through the analysis of figure 2.4 it is possible to conclude that the volume ratio is bigger than the power ratio. This means that if a 4 module machine is compared with a single machine configuration, the power in each module will be 25% of the single configuration machine power. However, the dimensions of each module will be approximately 35%, this means that the total volume occupy by the 4 modules will be bigger than the volume occupied by the single machine configuration, for the same power.

2.5.1 Joule Losses

The next step is to analyse the joule losses considering the modular configuration.

According to (2.32), the joule losses in one module is related to its volume as,

$$P_{Jm} \propto l_m^3 \quad (2.32)$$

and, using (2.32) and (2.29), we derive at

$$P_{JmT} \propto n l_m^3 \propto n^{0,25} l^3 \quad (2.33)$$

where P_{JmT} is the sum of each module joule losses.

The relation that enable the comparison between joule losses in a modular configuration and in a singular configuration is given by equation (2.34),

$$\frac{P_{JmT}}{P_J} \propto \frac{l^3 n^{0,25}}{l^3} \propto n^{0,25} \quad (2.34)$$

where P_J is the joule losses in a single machine. With equation (2.35), the efficiency can be computed

as

$$\eta_{mT} = \frac{1}{1 + \frac{n^{0.25} P_J}{P_N}} \quad (2.35)$$

Figure 2.5 shows the relationship between the total modular efficiency with respect to the number of models. In this figure, the efficiency of the single machine is considered to be $\eta = 91\%$.

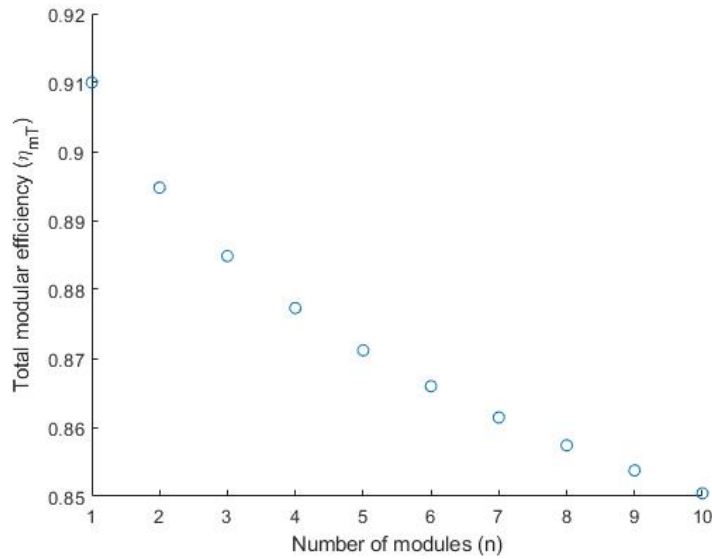


Figure 2.5: Relation between total module efficiency η_{mT} and the number of modules n

It is possible to conclude that the module configuration shows a decreasing in efficiency with the increasing of number of modules, this is a major drawback in module configuration when compared with singular configuration.

2.5.2 Temperature Dependence

Considering the temperature elevation constraints ($\Delta\theta=\text{cte}$), the equation(2.29) becomes,

$$P_{\theta m} = \frac{P_{\theta}}{n} \quad (2.36)$$

where $P_{\theta m}$ is the power that corresponds to one of the modules considering temperature constraints and P_{θ} the total power of the original drive system with only one machine considering temperature constraints. Assuming (2.28), the relation for the number of modules if given by

$$n = \left(\frac{l_{\theta}}{l_m} \right)^{\frac{7}{2}} \quad (2.37)$$

The ratio $\frac{V_m}{V}$ is given by equation (2.38)

$$\frac{V_m}{V} = \frac{1}{(\sqrt[7]{n})^6} \quad (2.38)$$

In figure 2.6 is represent the volume ratio, considering temperature constraints or not, and the power ratio.

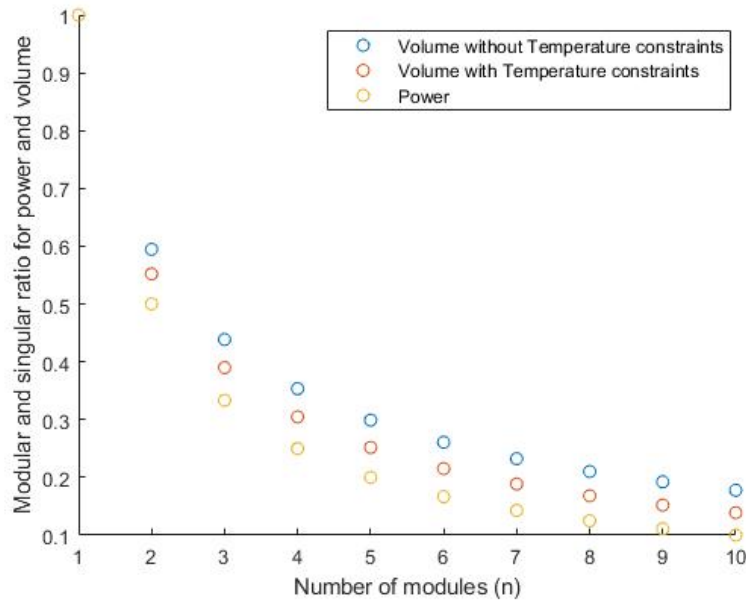


Figure 2.6: Relation between total module efficiency η_{mT} and the number of modules n

It is possible to conclude that in fact, the temperature constraints reduce the volume of each module however, the sum of them remains bigger than the volume of a single machine configuration.

Considering (2.27), the joule losses in each module with temperature constraints are find through

$$P_{Jm} \propto \frac{l_\theta}{l_m} J_\theta^2 r_m^3 \propto n^{-\frac{4}{7}} J_\theta^2 r_\theta^3 \quad (2.39)$$

The sum of each module joule losses is given by,

$$P_{JmT} \propto n^{\frac{3}{7}} J_\theta^2 r_\theta^3 \quad (2.40)$$

and with this relation, a similar to (2.34) can be defined

$$\frac{P_{JmT}}{P_J} \propto n^{\frac{3}{7}} \quad (2.41)$$

Figure 2.7 shows the relationship between the total modular efficiency with respect to the number of models for a situation with temperature constraints and without. In this figure, the efficiency of the single machine is considered to be $\eta = 91\%$.

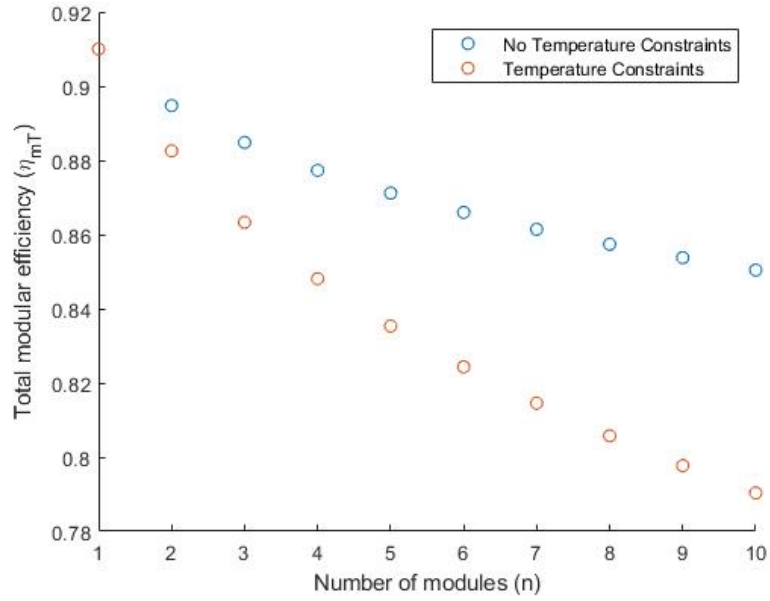


Figure 2.7: Relation between total module efficiency η_{mT} and the number of modules n

It is possible to conclude that with the increasing of modules, the solution without temperature constraints shows higher values of efficiency when compared with the solution with temperature constraints. The explanation for this is due to the fact that with temperature constraints the volume of each module is smaller for the same power and efficiency, this decreases the dissipative area with leads to an increases of joule losses for maintain the temperature in a constant value.

Chapter 3

High Temperature Superconductors

This chapter provides a summary of high temperature superconductors characteristics, describing their behaviour, the electromagnetic model used and the respective losses.

3.1 Introduction

At the beginning of 20th century, H. K. Onnes found that when certain materials are cooled below a transition temperature (4.2 K) they showed no resistance with current flowing through them. This was the major characteristic that defined superconductor materials during several decades until 1933 when W. Meissner and R. Ochsenfeld discover the Meissner effect, which showed that a superconductor is almost a perfect diamagnet. Later, it was discovered that some composites, could be superconductive with temperatures as high as 35 K. This results marked the first steps to the development of high-temperature superconductors (HTS). Nowadays, the temperatures of superconductive state of some materials are around 100 K, such as the YBaCuO (YBCO) composite, used in this dissertation, and liquid Nitrogen can be used (boiling point of 77 K) to refrigerate. During the last years, it was discovered that superconductors can be divided in type-I and type-II. Type-I superconductors are the ones that need temperatures below 30 K to be superconductive [7] [8]. In this dissertation, the main focus will be the type-II, also called HTS.

3.2 Maxwell's equations

The principles of this model stand on Maxwell's equations in a quasi-stationary regime, neglecting the displacement current vector $\frac{\partial \mathbf{D}}{\partial t}$, since the capacitive effects are negligible. Maxwell's equations are presented in the differential form in (3.1), (3.2), (3.3) and (3.4)

$$\nabla \cdot \mathbf{E} = \frac{\rho_q}{\epsilon_0} \quad (3.1)$$

$$\nabla \times \mathbf{E} = -\frac{\partial \mathbf{B}}{\partial t} \quad (3.2)$$

$$\nabla \cdot \mathbf{B} = 0 \quad (3.3)$$

$$\nabla \times \mathbf{H} \approx \mathbf{J} \quad (3.4)$$

where \mathbf{E} is the electric field vector, ρ_q is the total charge density, ϵ_0 is the permittivity of free space, \mathbf{B} is the magnetic flux density vector, \mathbf{H} is the magnetic field strength vector and \mathbf{J} is the current density vector [3]. Besides those four equations and to completely solve them, two isotropic constitutive relations, equation 3.5 and 3.6, can be established

$$B = \mu H \quad (3.5)$$

$$J = \sigma E \quad (3.6)$$

where μ is the magnetic permeability and σ is the electrical conductivity.

3.3 E-J Power Law for HTS

In normal conductors, the constitutive relationship between the electric field, \mathbf{E} , and the current density, \mathbf{J} , is a proportional one, being the proportionality constant the conductivity, σ , of the material.

In type II superconductors, the relation between \mathbf{E} and \mathbf{J} is non-linear and is defined by

$$E = E_0 \left(\frac{J}{J_C} \right)^m \quad (3.7)$$

where E_0 is the electric field that defines the critical current density, m is the power constant and J_C is the critical current density, which depends on the magnetic field density inside the superconductor, as well as its temperature [7].

Figure 3.1 shows the variation of the current density ratio with the electric field for different m parameter values.

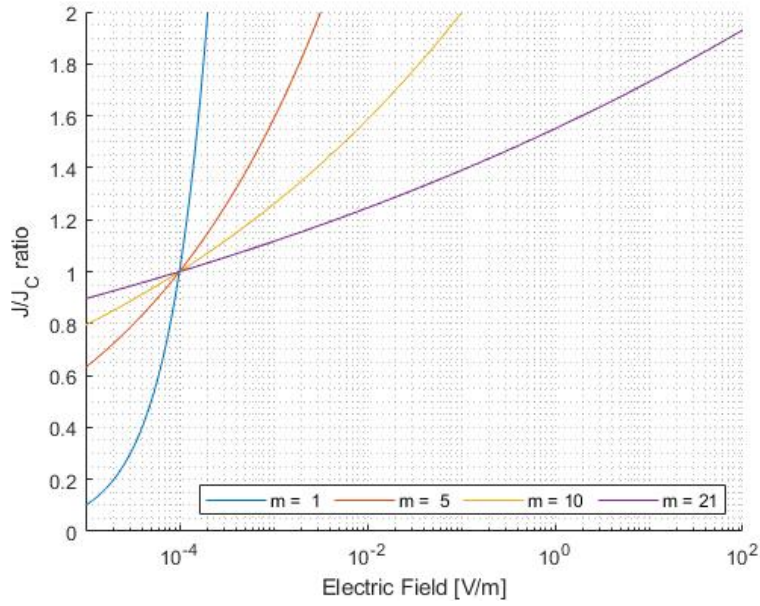


Figure 3.1: Dependency of the electric field with relative current density and m parameter at a logarithmic scale.

As said previously, the critical current, J_C , is dependent of the magnetic flux density distribution inside the superconductor, and the temperature, as equation 3.8 shows,

$$J_C = J_{C0}(T, T_C) \frac{B_0}{B_0 + B} \quad (3.8)$$

where J_{C0} represents the maximum critical current density of the material, dependent on temperature and critical temperature, B_0 represents the value of the applied magnetic flux density that reduces the value of the critical current density to half of its maximum value, and B is the norm of the magnetic flux density vector [3].

Figure 3.2 shows the critical current density and maximum critical current ratio with the increase of magnetic flux density, B , for different values of B_0 .

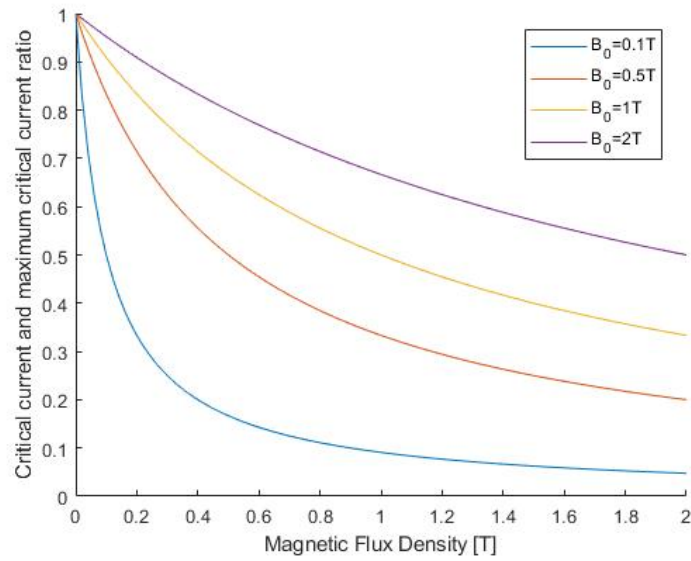


Figure 3.2: Critical current density and maximum critical current ratio in function of applied magnetic flux density for different values of B_0

The dependence of J_{C0} with the temperature, T , and critical temperature, T_C , is stated as

$$J_C(B, T) = J_{C0}(T, T_C) \left[\frac{B_0}{B_0 + B} \right] = J_{C0\beta} \left(1 - \left(\frac{T}{T_C} \right)^2 \right)^{\frac{3}{2}} \left[\frac{B_0}{B_0 + B} \right] \quad (3.9)$$

where $J_{C0\beta}$ represents the critical current density at 0 K with no applied field [3].

In figure 3.3 is shown the relationship between the critical current density ratio, $\frac{J_{C0}}{J_{C0\beta}}$, and the temperature ratio, $\frac{T}{T_C}$.

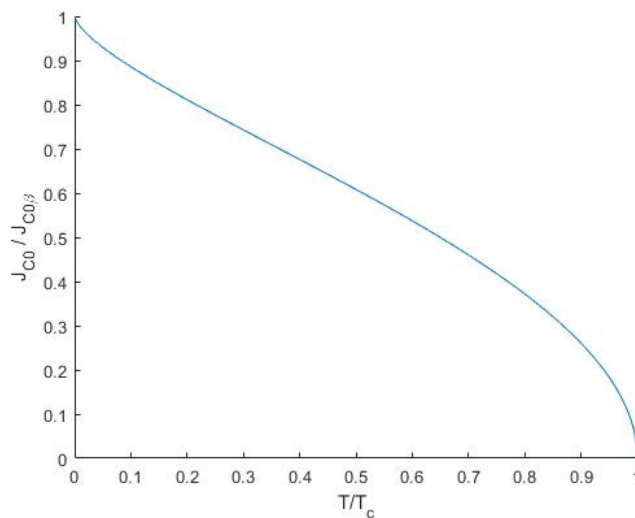


Figure 3.3: Critical current density and maximum critical current ratio in function of applied magnetic flux density for different values of B_0

The critical temperature, T_C , is also affected by the magnetic flux density inside the superconductor, being

$$T_C(B) = T_{C0}e^{-\frac{B}{30}} \tag{3.10}$$

where T_{C0} is the critical temperature when $B = 0$. Figure 3.4 shows the critical temperature variation with the magnetic flux density [3].

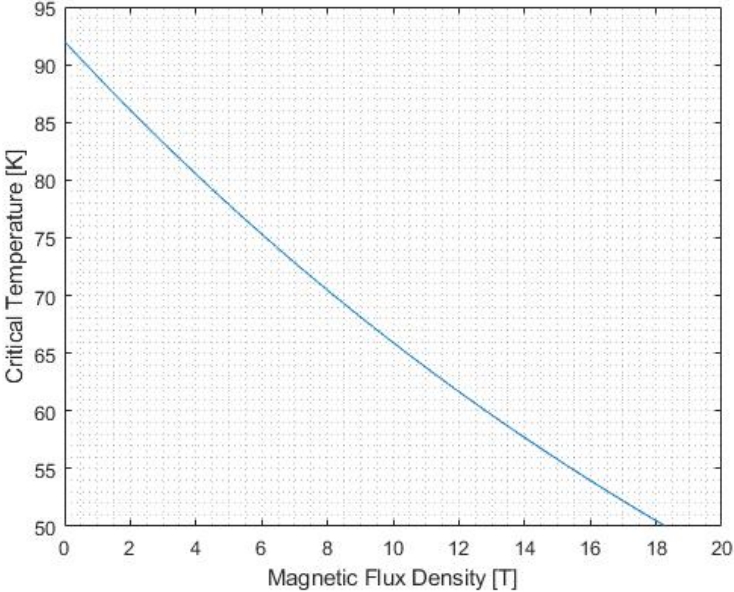


Figure 3.4: Critical temperature dependency with magnetic flux density

3.4 Critical Region and Superconductor Type

The superconductor state in a certain material is characterized by three parameters, the critical temperature T_C , the critical magnetic field H_C or the critical magnetic flux density B_C and the critical current density J_C . These parameters only can be exceeded locally otherwise the material loses his superconductivity state. Figure 3.5 shows the surface defining the superconductive region [7].

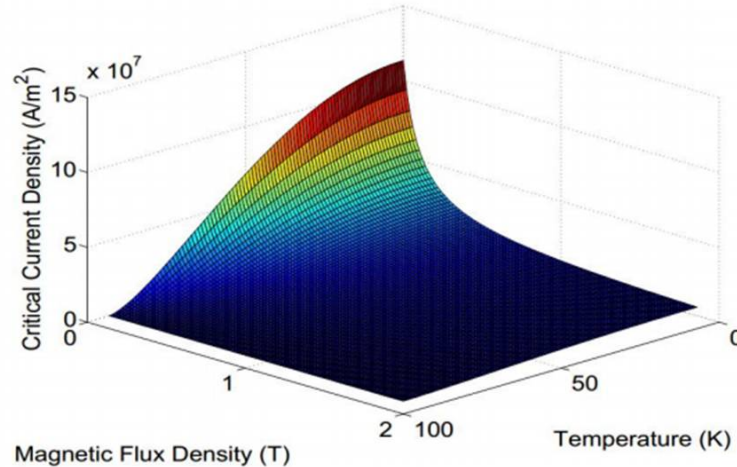


Figure 3.5: 3D graph defining superconductive region [3].

There are two types of superconductors. The type I is characterized by having one critical magnetic flux density field value, B_C , that when is surpassed, leads the material to lose its superconductivity. Another characteristic of type I is the absence of magnetic flux density inside the superconductor, meaning that the magnetization field, \mathbf{M} , is opposing the magnetic field, \mathbf{H} , inside the superconductor [3]

$$\mathbf{B} = 0 \rightarrow \mathbf{M} = -\mathbf{H} \quad (3.11)$$

$$\mathbf{B} \neq 0 \rightarrow \mathbf{M} = -\mathbf{H} \quad (3.12)$$

Figure 3.6 represents the magnetization in a type I superconductor. As expected, the magnetization function behaves like a straight line, $\mu_0 H$, until it reaches the critical magnetic flux density, B_C , and after that the magnetization is zero, losing is superconductivity.

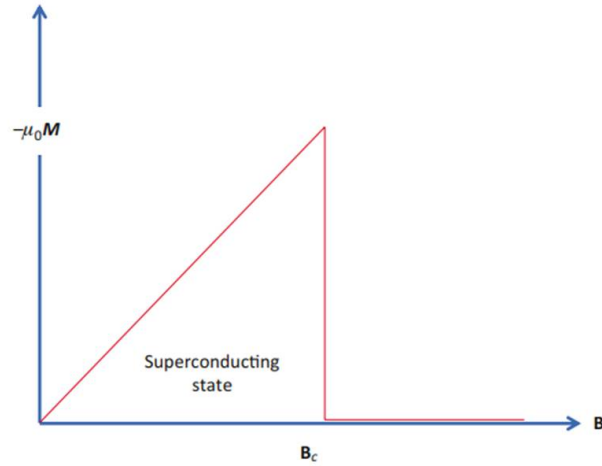


Figure 3.6: Magnetization of a type I superconductor [10]

In type II superconductors, it is necessary to consider two critical fields, the lower critical field B_{C1} and the upper critical field B_{C2} higher than B_{C1} . Until B_{C1} , the superconductor behaves as a type I. Above B_{C1} the magnetic flux density starts to penetrate the superconductor. A vortex is a magnetic flux quantum that penetrates the superconductor. Where the vortex appears the superconducting order parameter drops to zero. In this region, the material is no longer a superconductor and a current starts to circulate the vortex. Even though the vortices have formed, the rest of the material stays superconducting [9]. If the field surpassed the second critical field B_{C2} the material stops to be superconductive.

Figure 3.7 represents the magnetization of a type II superconductor.

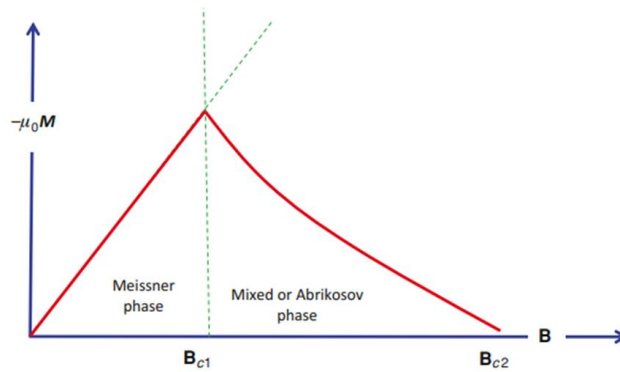


Figure 3.7: Magnetisation of a type II superconductor [10]

Finally, it is important to emphasize that B_{C2} is usually a lot bigger than B_C that's why type II superconductors are typically used for superconducting magnets [9].

3.5 Meissner effect and flux pinning

The Meissner effect exist in type I superconductor for B lower than B_C and for type II superconductor for B lower than B_{C1} . This effect is characterized by repelling all the magnetic field that tries to penetrate the superconductor (diamagnetic state). This happens because induced currents are created inside the material, that generates a magnetization that expels the external magnetic field as shown in figure 3.8 [7].

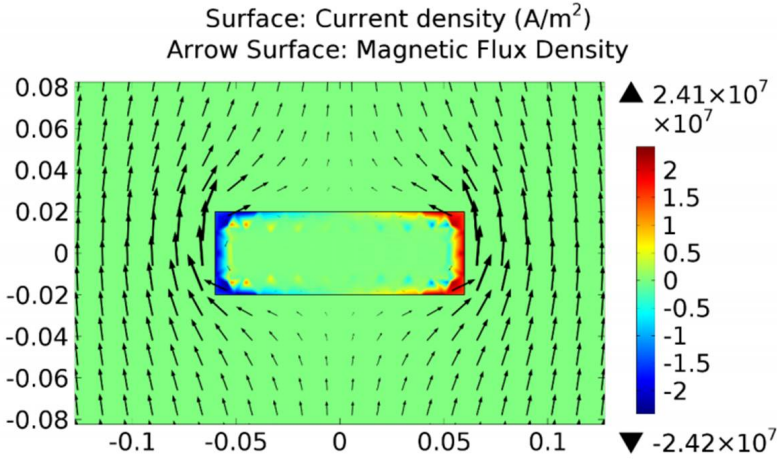


Figure 3.8: Example of meissner effect [3]

In type II the same occurs until B_{C1} , above that enters in the mixed state, where the magnetic field lines penetrate the superconductor in non superconductive regions, where impurities exist, and microscopic tubes are created, allowing the concentration of a magnetic flux (vortices) [7].

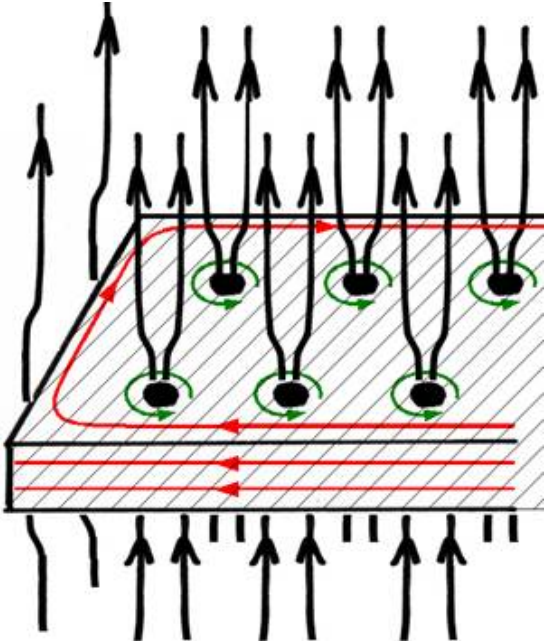


Figure 3.9: Example of Flux Pinning [11]

3.6 Joule Losses

For conductor materials, and using equation 2.12, the proportional relation of joule losses is given by,

$$P_J \propto \rho(T)J^2 \quad (3.13)$$

where $\rho(T)$ is the electrical resistivity in function of temperature.

This same relation can be found for YBCO as presented in [7] but in this case, using equations 3.7 and 3.8, the electric field in function of current density is given through equation 3.14,

$$E = \frac{E_0}{J_{C0}} \left(\frac{B_0 + B}{B_0} \right)^m \left(\frac{J}{J_{C0}} \right)^{(m-1)} J \quad (3.14)$$

and the resistivity of YBCO can be considered as

$$\rho_{YBCO} = \frac{E_0}{J_{C0}} \left(\frac{B_0 + B}{B_0} \right)^m \left(\frac{J}{J_{C0}} \right)^{(m-1)} \quad (3.15)$$

Next step is to make a qualitative comparison between losses in YBCO and the losses in a regular conductor material such as copper. To achieve that, it is necessary to know how the resistivity of copper changes with temperature and that is found through equation 3.16

$$\rho(T) = \alpha(T_0)\rho(T_0)(T - T_0) + \rho(T_0) \quad (3.16)$$

where $\rho(T_0)$ is the resistivity at reference temperature T_0 , $\rho(T)$ is the resistivity at temperature T and $\alpha(T_0)$ is the temperature coefficient (for $T_0=20^\circ\text{C}$ is 3.9×10^{-3}).

Figure 3.10 shows the comparison between the copper and YBCO resistivities for temperatures between 40 K and 91 K with $B = 0.1$ T, $J = J_c$ and the values for YBCO presented in table 3.1.

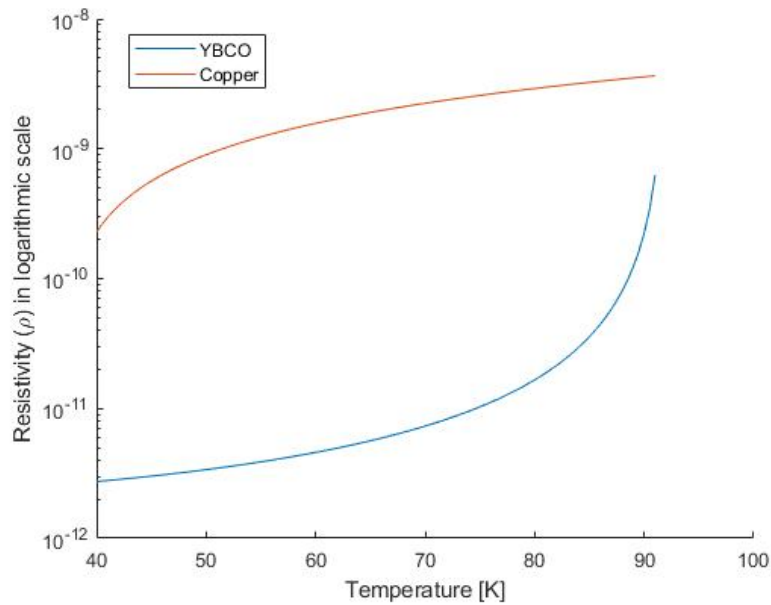


Figure 3.10: Resistivity in a logarithmic scale in function of Temperature

Table 3.1: Parameter values for YBCO [14]

Parameter	YBCO
m	21
$E_0 [Vm^{-1}]$	10^{-4}
$B_0 [T]$	0.1
$T_{C0} [K]$	92
$J_{C0\beta} [Am^{-2}]$	1.134×10^8

Is perceptible that in general, the resistivity of copper is one hundred times bigger than the resistivity of YBCO except when the temperature approaches the boundary temperature of superconductivity for YBCO ($T=93K$).

To understand how this affects the temperature of an object made by copper or YBCO, heat conduction and convection need to be considered. For that will be considered the internal heat generation in a massive cylinder in stationary regime [15]. This is a good approximation to the internal heat generated through joule effect due to electrical current. Starting with the general heat conduction equation

$$\nabla^2 T + \frac{q_G}{k} = \frac{1}{\alpha} \frac{\partial T}{\partial t} \quad (3.17)$$

Using the Laplacian for cylindrical coordinates,

$$\nabla^2 T = \frac{1}{r} \frac{\partial}{\partial r} \left(r \frac{\partial T}{\partial r} \right) + \frac{1}{r^2} \frac{\partial^2 T}{\partial \phi^2} + \frac{\partial^2 T}{\partial z^2} \quad (3.18)$$

To simplify the calculations, it will be consider as hypothesis a radial symmetry ($\frac{\partial^2}{\partial \phi^2} = 0$) and a very long cylinder compared to the radius ($\frac{\partial^2}{\partial z^2} = 0$). Introducing this simplifications in 3.18,

$$\frac{1}{r} \frac{d}{dr} \left(r \frac{dT}{dr} \right) + \frac{q_G}{k} = 0 \quad (3.19)$$

and integrate both sides of the equation,

$$T(r) = -\frac{q_G r^2}{4k} + C_1 \ln(r) + C_2 \quad (3.20)$$

the expression for temperature in function of radius is found. The next step is to find the constants C_1 and C_2 . To do that is necessary to define conditions, the first one saying that the temperature at the cylinder's wall is known ($T(r = r_0) \rightarrow T_W$), the second is to assume that in the centre of the cylinder, the variation of temperature is 0 ($\frac{dT}{dr} = 0$ in $r=0$). Finally, the heat conduction equation becomes,

$$T(r) = \frac{q_G}{4k} (r_0^2 - r^2) + T_W \quad (3.21)$$

in which q_G are the joule losses per volume, k the thermal conductivity, r_0 the cylinder radius and T_W the temperature at the cylinder's wall.

Another consideration that should be taken into account is the temperature in the walls of the cylinder due to convection. The equation 3.22 show this relation

$$T_W = T_{out} + \frac{P_J}{hA} \quad (3.22)$$

where T_{out} is the temperature that surrounds the cylinder, P_J is the power due to joules effect, A is the surface area and h is the thermal transfer coefficient.

Considering a copper and YBCO wire with a radius of 0.89 mm and a length of 1 m, table 3.2 gives the comparative values of losses and increase of temperature for different situations with $h = 10 \text{ Wm}^{-2}\text{K}^{-1}$, $A = 5.59 \times 10^{-3} \text{ m}^2$ (values for air). The variation of temperature inside the cylinder will be considered negligible, since the cross-section is extremely small, leading to a wall temperature very similar to the center temperature and the variation of temperature in the cylinder walls will be given by ΔT_W .

Table 3.2: Wall Temperature increase for different situations

Material	Current Density [A/m^2]	Joule Losses [W]	ΔT_W [$^{\circ}C$]
Copper (Air Temperature)	9.07×10^6	3.52	62.96
Copper (Cooled at 77K)	9.07×10^6	5.5×10^{-1}	9.83
YBCO	9.07×10^6	2.2×10^{-3}	0.04

As it can be seen in table 3.2, the cooled copper has a temperature increasing of only 15.16% when compared with the temperature increasing at air temperature. However, the YBCO has a temperature increasing of 0.41% when compared with copper cooled, showing an increase of temperature almost imperceptible, making this material a better solution than the copper for solution where is necessary high values of current density.

3.7 KIM Electromagnetic Model

3.7.1 Introduction

Considering an external magnetic field, H_a , defined as (3.23)

$$H_a = H_m \sin(\omega t) \quad (3.23)$$

where H_m is the amplitude of the waveform, ω the angular frequency and t time.

This external magnetic field is applied uniformly to an HTS bulk along the z axis, like shown in figure 3.11.

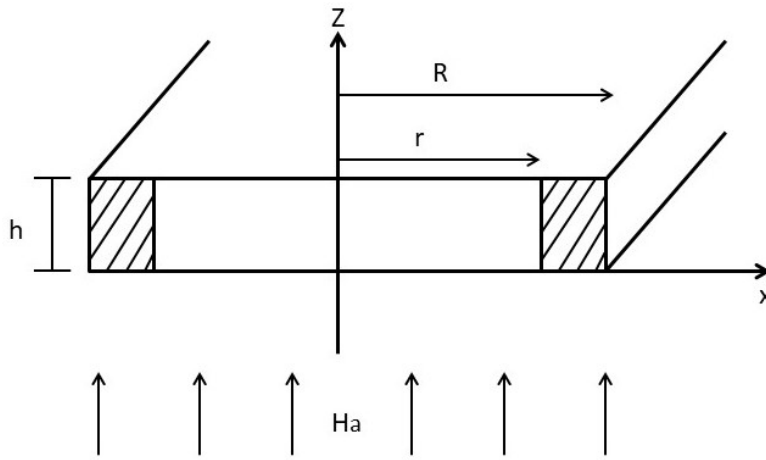


Figure 3.11: Superconductor bulk representation

In this configuration, the magnetic quantities have only z components, and the induced currents have only x and y components. This model involves only macroscopic induced currents, magnetization, flux density, and field.

The applied magnetic field, H_a , is defined as

$$H_a = \frac{B}{\mu_0} \quad (3.24)$$

where B is the macroscopic flux density and μ_0 is permeability of free space. If H_a is the applied magnetic field and M_i is the local magnetization, that is, the field produced by bulk induced currents, the equation (3.25) relates these variables with H , the local magnetic field inside the bulk [12]

$$H = \frac{B}{\mu_0} + M_i \quad (3.25)$$

The total magnetization M is the average of M_i over the sample cross section.

The induced currents density J , the H and the M_i along a given circuit are uniform and are written as functions of x : $J(x)$, $H_i(x)$, and $M_i(x)$.

The magnetization $M_i(x)$ can be found through (3.26)

$$M_i(x) = \int_r^R J_i(x) dx \quad (3.26)$$

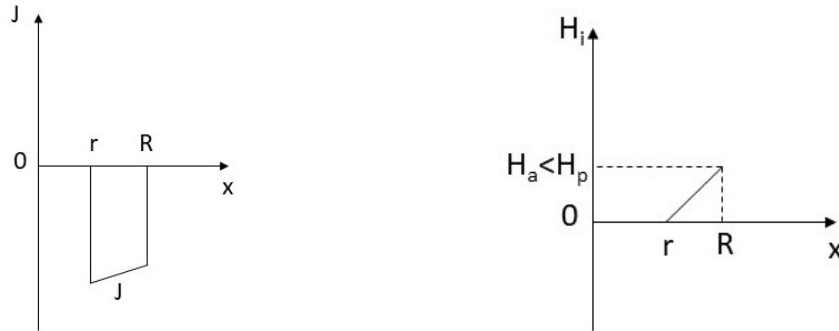
The $J(x)$ is given through (3.27)

$$J(x) = \frac{sgn(J)k_1}{\sqrt{(H_0)^2 - sgn(JH_i)2k_1(x+c)}} \quad (3.27)$$

where c is an integration constant to be determined by the boundary conditions and where k_1 and H_0 are constants.

If the length and width of the cross-section are the same, can be approximated to a cylindrical specimen of radius a , where the area is πa^2 and the differential area element is $2\pi x dx$ and the height is a too. This cylindrical geometry will be used in the implementation (subsection 3.7.2) due to the simplification of variables [12].

Considering the initial state, where $H_a = M = 0$, and consider the increase of H_a in z direction. According to Faraday's Law (3.2), the induced currents J , with negative sign, will penetrating the bulk from the surface inward. Considering now that these induced currents only penetrates until a certain $x = r$, this means that the local internal field, H , in the bulk will be H_m at $x = R$, decreasing to 0 until $x = r$ and remains in that value for $x < r$, as figures 3.12(a) and 3.12(b) exemplify [12].



(a) Induced current in function of x

(b) Magnetic field inside bulk in function of x

Figure 3.12: Schematic representations of KIM model current and magnetic field behaviour

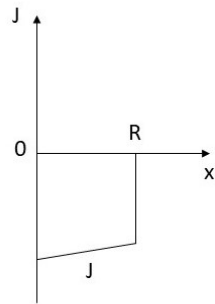
If the value of H_m increases, r will be decrease. This means that when $r = 0$, the bulk is completely full-penetrated and H_p is the corresponding field, as can be seen in figure 3.13(a) and 3.13(b) [12].

The value of H_p is defined as

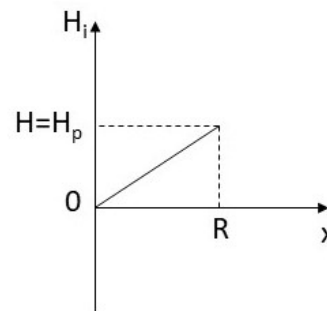
$$H_p = \sqrt{(H_0)^2 + 2k_1 R} - H_0 \quad (3.28)$$

where R is the radius of the cylindrical YBCO and k_1 is a variable that depends on the temperature.

The shaded part in 3.11 represents the area where the induced currents are formed by the external magnetic field, H_a .



(a) Induced current in function of x



(b) Magnetic field inside bulk in function of x

Figure 3.13: Schematic representations of KIM model current and magnetic field behaviour

Using Ampere Law, equation 3.4, in the area where are the induced current, equation 3.29 can be developed,

$$H = J_C(R - r) \quad (3.29)$$

where J_C represents the critical current for this superconductor and H is the internal magnetic field [12].

Equation 3.29 can be written as,

$$H = J_{C0} \frac{H_0}{H_0 + H} (R - r) \quad (3.30)$$

if the temperature is considered negligible. To allow an analysis between the radius of penetration, r , and the applied magnetic field, the equation 3.30 will be rearranged as,

$$H^2 + H_0 H - k(R - r) = 0 \quad (3.31)$$

where $k = H_0 J_{C0}$.

In figure 3.14 is represented the variation of penetration in function of the internal magnetic field for standard YBCO values and for a bulk radius of 2 cm.

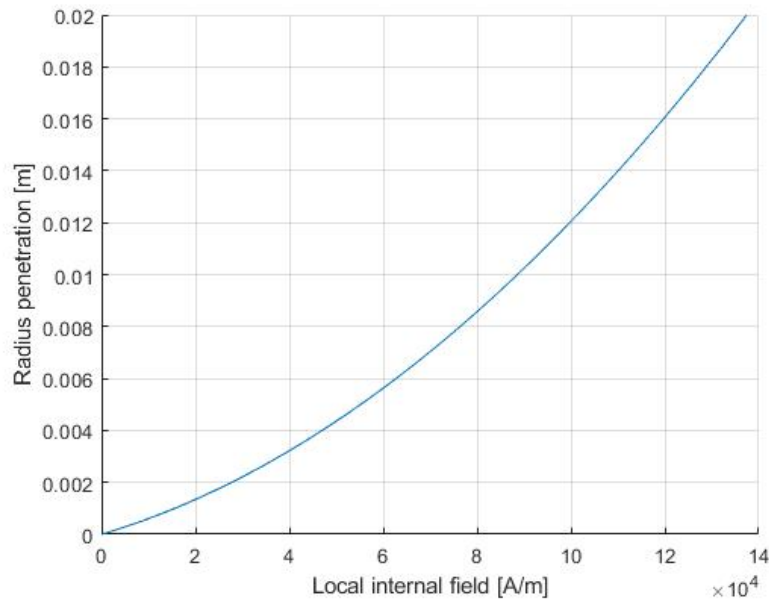


Figure 3.14: Bulk penetration in function of the internal magnetic field

For $H_i = 1.37 \times 10^5$ all bulk have within induced currents, for this $H_m = H_p$.

3.7.2 Implementation

Through the software MATLAB, it was developed a code, that can generate the M-H curve for different radius dimension and for different external magnetic fields. Additionally, the code presents in real time the variation of $J_i(x)$ and $B_i(x)$ in function of the radius when a magnetic flux density, $B_a(t)$, is applied as shown in figure 3.15.

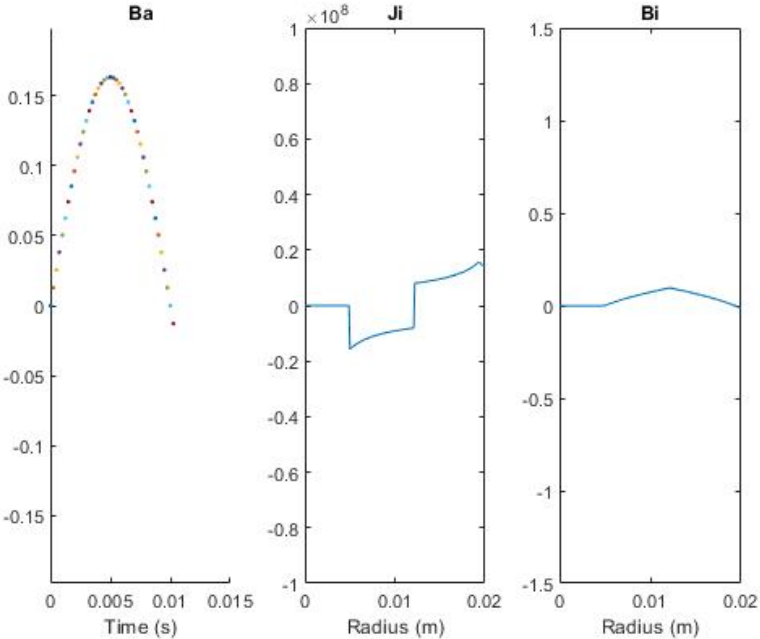


Figure 3.15: Figure from Matlab code for M-H analytic curve

In terms of M-H curves is important to note that when the amplitude of the external magnetic field is lower or equal to H_p the shape of the curve have a characteristic shape as in figure 3.16.

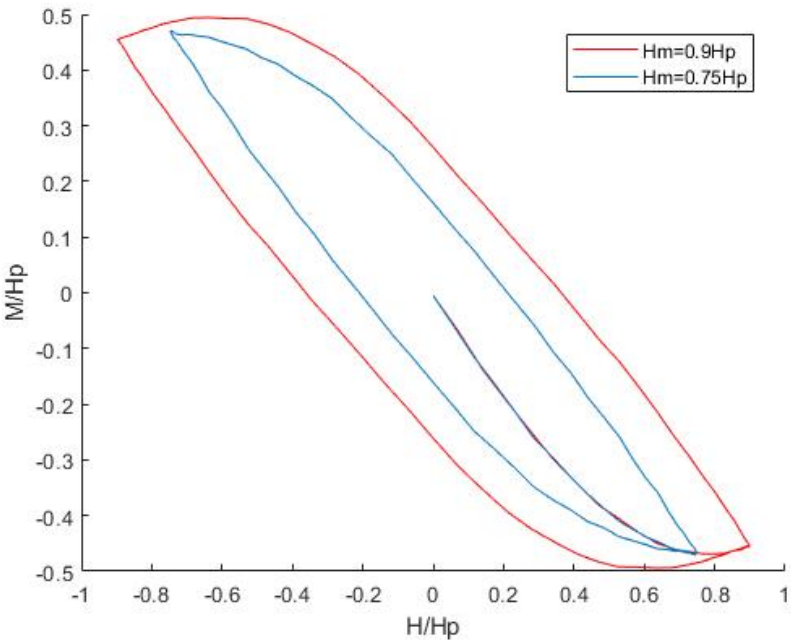


Figure 3.16: M-H curve for external magnetic field amplitude's lower than H_p

When the external magnetic field is higher than H_p , the M-H starts to change the shape, like figure 3.17 shows.

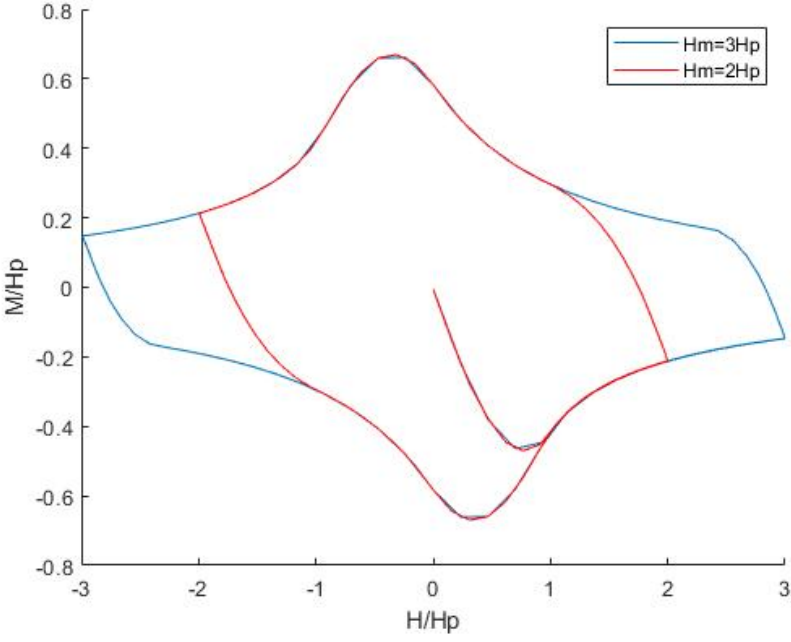


Figure 3.17: M-H curve for external magnetic field amplitude's higher than H_p

3.8 Hysteresis Losses

3.8.1 Introduction

In the electromagnetic model considered, the hysteresis losses will be associated with H_i and its variation when subject to a time-variant external applied magnetic field, H_a . To compute the hysteresis loops for different values of H_m , it will be used the equations for $J_i(x)$ and $H(x)$ defined in (3.27) and (3.25).

The figure 3.18 is a YBCO generic M-H for $H_m \leq H_P$.

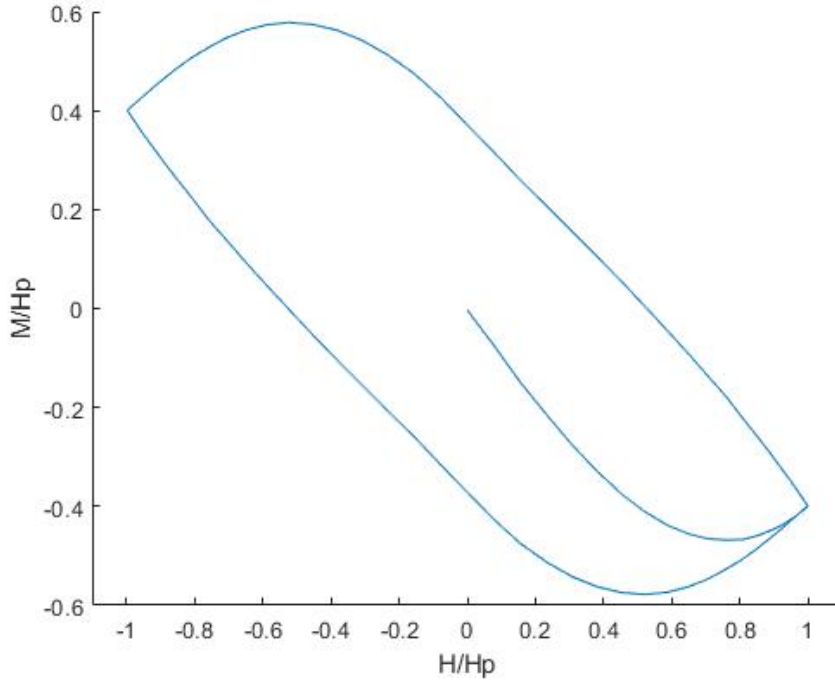


Figure 3.18: Generic M-H curve for YBCO, scaled by H_p , for $H_m \leq H_P$.

It is possible to see through 3.18 that the magnetization response to the applied magnetic field is different in YBCO and in a ferromagnetic material. In YBCO, when H_a increases, the magnetization decreases for negative values to cancel the imposed magnetic field inside the bulk. When H_a decreases, the magnetization increases until H_a increases again.

The total hysteresis losses will be calculated through the integration of the area inside the loop, as given in equation (3.32) [3]

$$W_H = \oint B dM = \oint \mu_0 H dM \quad [J/m^3/cycle] \quad (3.32)$$

The use of different frequencies is common, in this cases is necessary to see the result of 3.32 as a power density loss

$$P_H = f \oint B dM \quad [W/m^3] \quad (3.33)$$

3.8.2 Implementation Examples

Through the M-H curves generated with Matlab code and applied equation (3.32) it is possible to know the different losses for different radius or different applied magnetic fields.

Considering that the temperature remains the same, the increase of the radius dimensions leads to an increase in the value of H_p , this means that is possible to achieve higher magnetization than in smaller radius without changing the shape of the curve M-H.

In figure 3.19 is represented the M-H curves for different radius, r , for $H_m = H_p$.

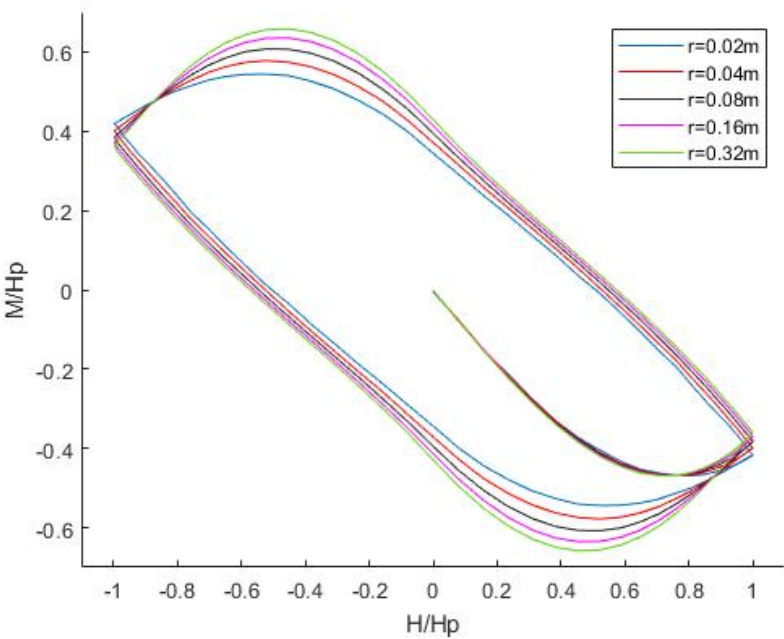


Figure 3.19: M(H) curves for different radius and for $H_m = H_p$

It is perceptible that exists an increase of occupied area by the curve M-H with the increase of radius size, this happens because the H_p increases with the increase of radius size, as equation (3.28) shown, leading to more magnetic field penetration, that reflects into an increase of magnetization inside the YBCO bulk.

Another relevant comparison is between how this increase of size affects the maximum magnetization value (M_{max}) and the hysteresis losses per cycle (W_h).

To understand the behaviour of these values and further quantify them, figure 3.20 is necessary because the conditions are the same that in figure 3.19 but the axis values aren't divided by H_p .

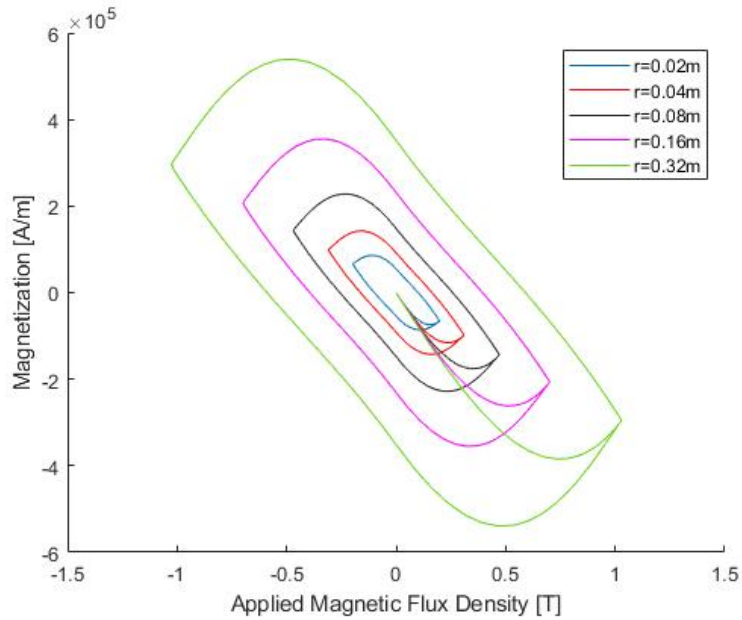


Figure 3.20: $M(B)$ curves with nominal values for $H_m = H_p$

In figure 3.21, is represent the normalized values of M_{max} and W_h in function of radius for $H_m = H_p$. Both variables are divided by the respective values when $r=0.02m$, this allows to focus only on the growth comparatively with the initial value ($r=0.02m$).

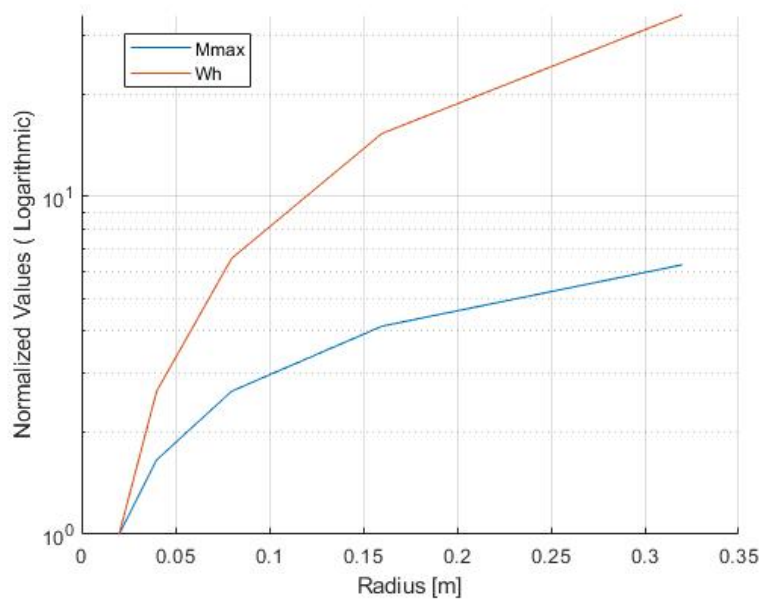


Figure 3.21: Normalized (logarithmic) curve for W_h and M_{max} in function of radius for $H_m = H_p$

It is possible to conclude that for a constant value of penetration, the increasing of the radius leads to a bigger increase in the hysteresis losses than in the maximum magnetization value. Another conclusion that can be taken is that the growth rate of W_h is bigger for small radius variation than for bigger ones, leading to conclude that can exist a certain benefit in efficiency with the increase of size.

The next step is study the relation of hysteresis losses with the increasing of radius and magnetic penetration ($\frac{H}{H_p}$). Figure 3.22 represent this relation.

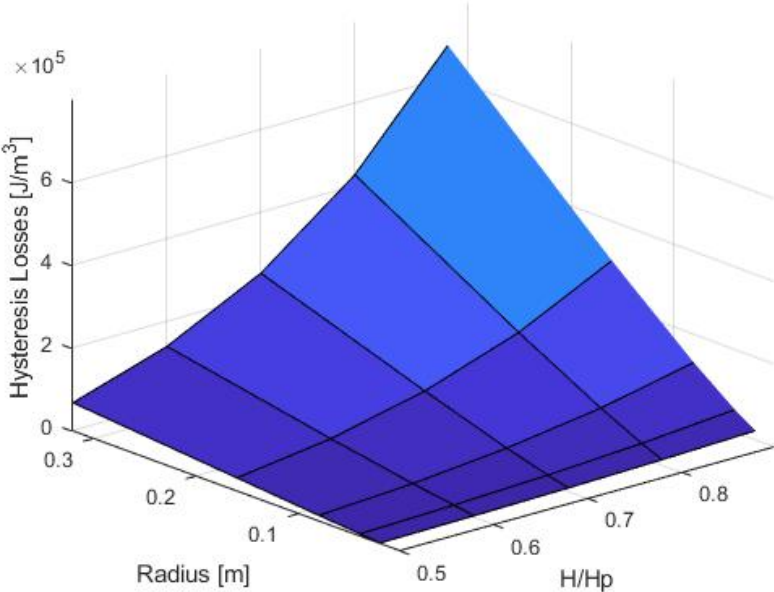


Figure 3.22: 3D plot for radius, ratio of penetration and hysteresis losses

As expected, the higher value for hysteresis losses occurs for the maximum ratio of magnetic penetration and for the maximum radius size.

Another relevant comparison is between different values of H_m . The figure 3.23 shows the curve $M(B)$ for different applied magnetic flux densities. It is perceptible that for $\frac{H}{H_p} < 1$ the shape of the curve is different than for $\frac{H}{H_p} > 1$ and the occupied area variation is bigger for the first scenario than the second.

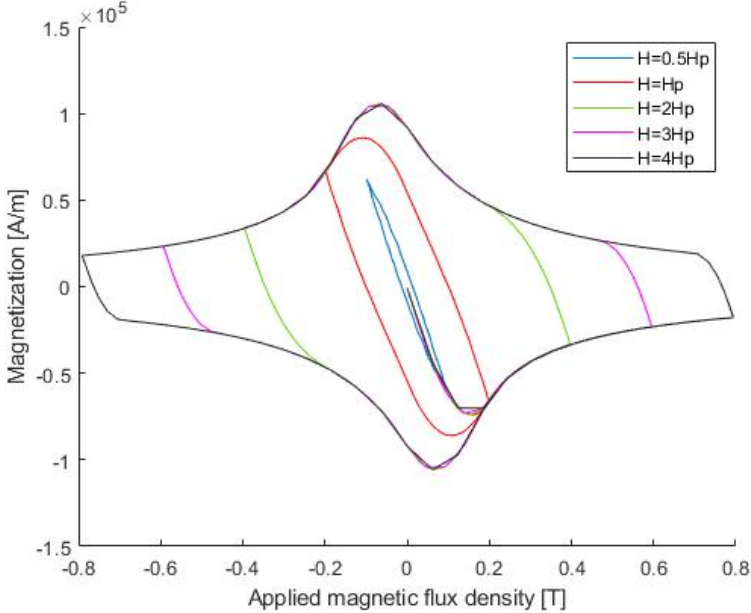


Figure 3.23: $M(B)$ curve for different ratio of penetration with $r=0.02m$

To confirm this perception, it is compute the logarithmic variation of W_h for different H_m . It is possible to conclude that the growth rate of W_h until $\frac{H}{H_p} = 1$ is much bigger than for $\frac{H}{H_p} > 1$.

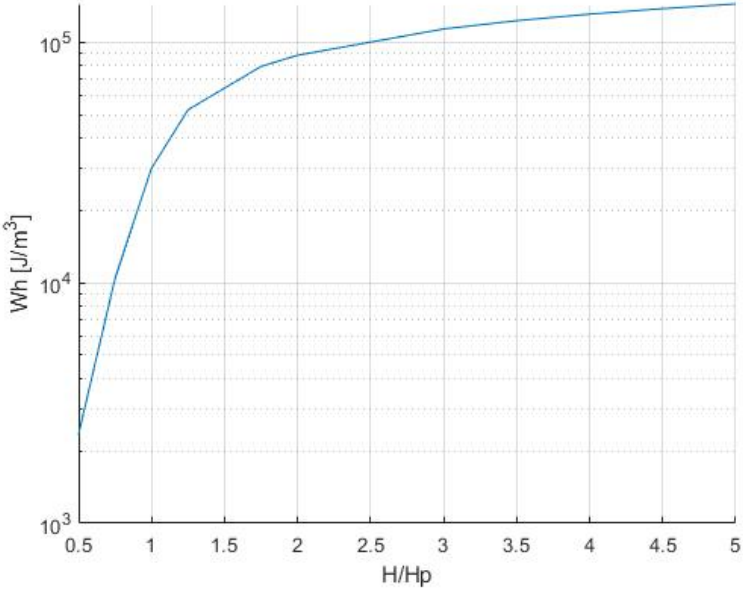


Figure 3.24: Hysteresis density losses at a cycle for different ratio of penetration (logarithmic scale) with $r=0.02m$

Temperature effect

The temperature has an important role in the values of the M-H curves as can be seen in figure 3.25.

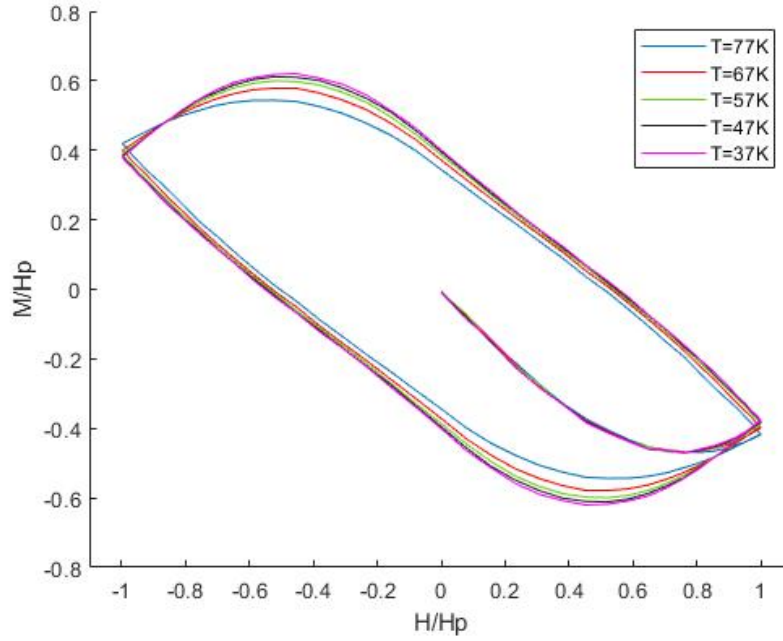


Figure 3.25: M(H) for different temperatures with $r=0.02\text{m}$

This happens because the variable k_1 , (3.28), depends on the temperature,

$$k_1 \propto \left[1 - \left(\frac{T}{T_c} \right)^2 \right]^{\frac{2}{3}} \quad (3.34)$$

where T_c is the critical temperature value defined as 92K. When the temperature decreases, the variable k_1 increases and this leads to an increase of H_p that enable to achieve higher values of magnetization inside the YBCO without changing shape.

This is very similar to the variation of M-H curves with radius. This happens because both r and k_1 affect H_p in the same way (equation 3.28). However, the figures 3.19 and 3.25 aren't exactly the same because when T varies between 77K and 37K, the value of k_1 increases until six times, instead when radius varies between 0.02 m and 0.32 m, the value of r increases sixteen times.

Chapter 4

Similitude Laws for YBCO

The main scope of this chapter is the application of similitude laws in YBCO material. It will be also made comparisons of efficiency between conventional machine designs and designs with YBCO bulks.

4.1 Magnetic density flux constant

This condition is a necessary condition to compare the behaviour of a machine with PM with a machine with YBCO bulks replacing the PM. It will be considered during this section that the average value of magnetic density flux in YBCO bulk is maintained constant.

4.1.1 Singular Configuration

Using the code in Matlab and the function "cumtrapz" it was possible to compute the total hysteresis losses, W_H , in a cycle (3.32) of any M-H curve. Figure 4.1 shows several acquired data for hysteresis losses in function of volume, always keeping the average value of magnetic density flux in YBCO bulk constant, and the correspondent fitting curve.

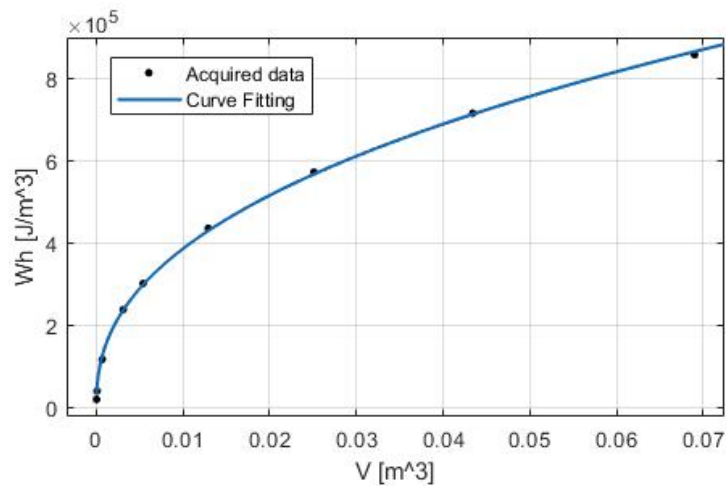


Figure 4.1: Acquired data for hysteresis losses in function of volume and the best curve fitting for the situation with magnetic flux constant

The equation that fits better the above points is give by,

$$W_h = 2.6 \times 10^5 \times V^{0,4175} \quad (4.1)$$

thus the variation of hysteresis losses with the volume is given by (4.2)

$$W_H \propto V^{0,4175} \quad (4.2)$$

From chapter 2, it is known that $V \propto r^3 = l^3$ and from chapter 3 it is known that $W_H \propto P_H$, so the final expression that relates the hysteresis losses with dimension is given by (4.3).

$$P_H \propto l^{1,253} \quad (4.3)$$

Considering the same conditions for P_N as in chapter 2

$$\frac{P_H}{P_N} \propto \frac{l^{1,253}}{l^4} \propto l^{-2,75} \quad (4.4)$$

The relation for the efficiency of YBCO in function of linear dimension is given by (4.5).

$$\eta_{YBCO} = \frac{1}{1 + \frac{K_1}{l^{2,75}}} \quad (4.5)$$

Figure 4.2 shows a comparison between the efficiency of a machine if only hysteresis losses in YBCO or only joule losses in the conductors are considered. It is important to remember that constant K_1 is defined to set the initial efficiency at 0.91.

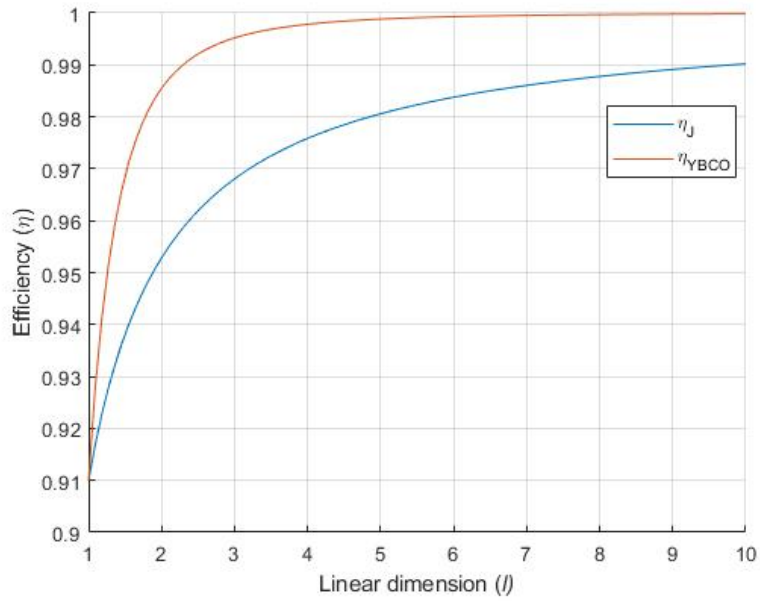


Figure 4.2: Efficiency comparison between YBCO and joule losses in conductors.

4.1.2 Modular Configuration

Based on subchapter 2.5, the YBCO hysteresis losses in each module is given by (4.6)

$$P_{Hm} \propto l_m^{1,253} \quad (4.6)$$

and the total modular hysteresis losses is given by (4.7)

$$P_{HmT} \propto n l_m^{1,253} \propto n^{0,687} l^{1,253} \quad (4.7)$$

To find an efficiency relation is necessary first relate the total modular hysteresis losses with the hysteresis losses for a singular configuration as show relation (4.8)

$$\frac{P_{HmT}}{P_H} \propto n^{0,687} \quad (4.8)$$

The respective efficiency of this modular configuration is give by relation (4.9).

$$\eta_{mT} \cong \frac{1}{1 + \frac{n^{0,687} P_H}{P_N}} \quad (4.9)$$

In figure 4.3 is represented the total modular efficiency as a function of the number of modules for the YBCO hysteresis losses when considered a singular configuration efficiency with $\eta = 91\%$.

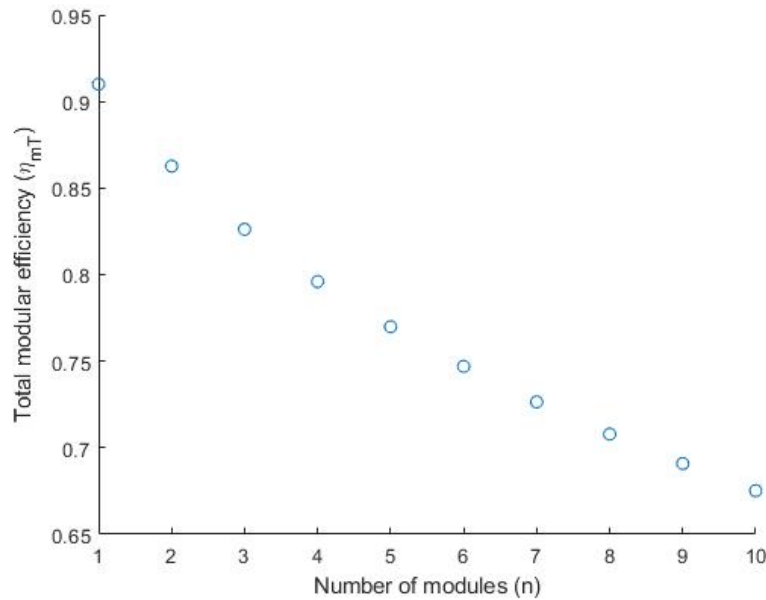


Figure 4.3: Modular efficiency in function of number of modules

In figure 4.4 is represented the comparison between the joule losses with temperature constraints and the hysteresis losses for YBCO in function of the number of modules when considered a singular configuration efficiency with $\eta = 91\%$.

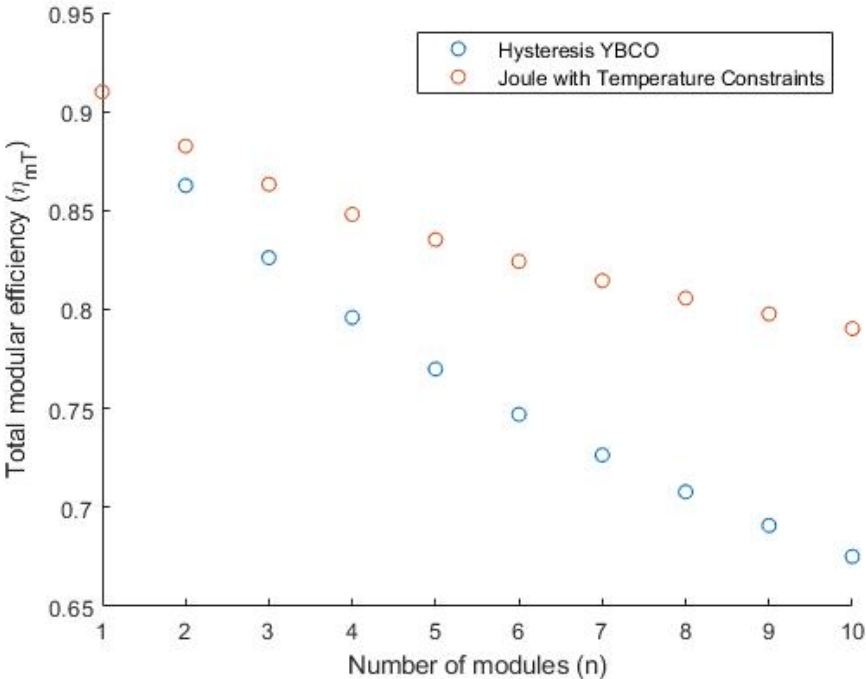


Figure 4.4: Comparison between the joule losses with temperature constraints and the hysteresis losses for YBCO in function of the number of modules

It is possible to conclude that the modular configuration for YBCO leads to a decreasing efficiency when compared with joule losses. This substantial decrease occurs because when the number of modules increases, there is a reduction in the linear dimension, for each module, but the magnetic flux density is constant in all, this leads to an increase in losses,(4.4), that leads to a decrease in efficiency.

4.1.3 Machine with YBCO as PM

In a machine with YBCO instead of PM, the equation 2.22 becomes

$$P_T = P_{iron} + P_{Jcoil} + P_{HYBCO} \quad (4.10)$$

Considering the analytic relation found in (4.3), the equation 4.10 becomes the relation

$$P_T \propto 3l^3 + l^{1,253} \quad (4.11)$$

Finally to compute the efficiency is necessary divide (4.11) through the nominal power

$$\frac{P_T}{P_N} \propto \frac{3}{l} + l^{-2,75} \quad (4.12)$$

The relation for the efficiency of a machine with YBCO in function of linear dimension is given by (4.13).

$$\eta_\alpha = \frac{1}{1 + K_1 \left(\frac{3}{l} + \frac{1}{l^{2,75}} \right)} \quad (4.13)$$

In figure 4.5 is represented the comparison between the efficiency of a machine with PM and a machine with YBCO instead of PM.

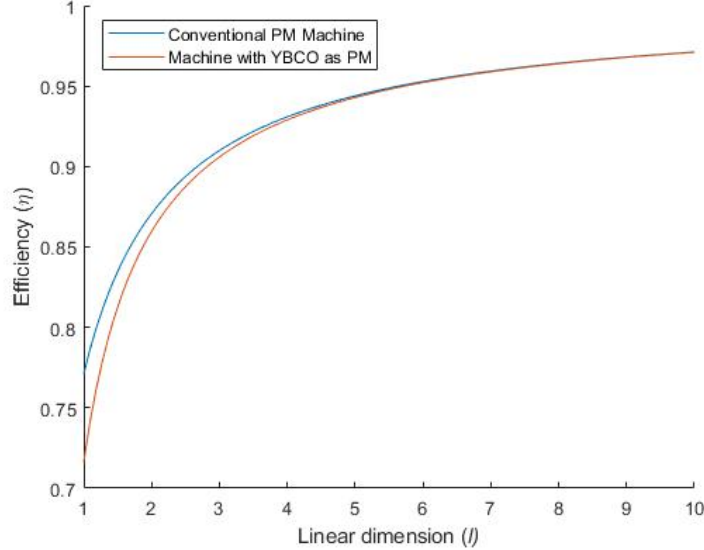


Figure 4.5: Efficiency for machine with PM and with YBCO

As it can be seen through figure 4.5, there is a smaller difference in efficiency between the conventional machines with PM and machines with YBCO. This difference decreases with the increase of linear dimension which leads to a convergence in efficiency of both machines. This was expected since for smaller linear dimension values the term P_{HYBCO} have some influence. However, with the increase of linear dimension, this term starts to lose his influence.

4.2 Current density constant

This condition is a necessary condition to compare the behaviour of a conventional PM machine with copper coils with a machine with YBCO replacing the copper coils. It will be considered during this section that the average value of current density in YBCO is maintained constant.

4.2.1 Singular Configuration

In figure 4.6 is shown the acquired data for hysteresis losses in function of volume and the best curve fitting for the situation with current density constant.

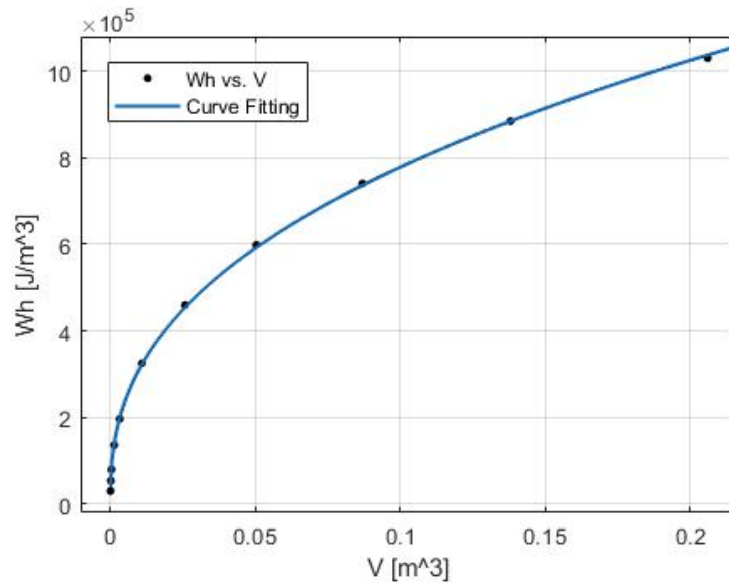


Figure 4.6: Acquired data for hysteresis losses in function of volume and the best curve fitting for the situation with current density constant

The equation that fits better the above points is give by (4.14),

$$W_h = 1.96 \times 10^6 \times V^{0,39} \quad (4.14)$$

thus the variation of hysteresis losses with the volume is given by (4.15)

$$W_H \propto V^{0,39} \quad (4.15)$$

The final expression that relates the hysteresis losses with dimension is given through (4.16)

$$P_{HJ} \propto l^{1,17} \quad (4.16)$$

Considering the same conditions for P_N as in chapter 2

$$\frac{P_{HJ}}{P_N} \propto l^{-2,83} \quad (4.17)$$

The relation for the efficiency of YBCO, considering current density constant inside, in function of linear dimension is given by (4.18).

$$\eta_{YBCOJ} = \frac{1}{1 + \frac{K_1}{l^{2,83}}} \tag{4.18}$$

Figure 4.7 shows a comparison between the efficiency of a machine if only hysteresis losses in YBCO or only joule losses in the conductors are considered, for density current constant.

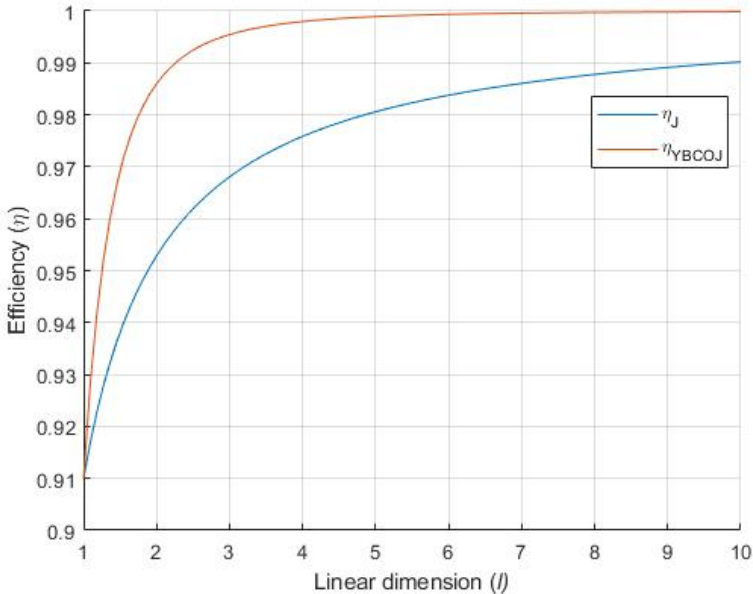


Figure 4.7: Efficiency comparison between YBCO and joule losses in conductors for density current constant

4.2.2 Modular Configuration

Based on subchapter 2.5, the YBCO hysteresis losses in each module is given by (4.19)

$$P_{Hm} \propto l_m^{1,173} \quad (4.19)$$

and the total modular hysteresis losses is given by (4.20)

$$P_{HmT} \propto n l_m^{1,173} \propto n^{0,708} l^{1,173} \quad (4.20)$$

To find an efficiency relation is necessary first relate the total modular hysteresis losses with the hysteresis losses for a singular configuration as show relation (4.21)

$$\frac{P_{HmT}}{P_H} \propto n^{0,708} \quad (4.21)$$

The respective efficiency of this modular configuration is give by relation (4.22).

$$\eta_{mT} \cong \frac{1}{1 + \frac{n^{0,708} P_H}{P_N}} \quad (4.22)$$

In figure 4.8 is represented the comparison between total modular efficiency of a machine where YBCO replaces the PM and a machine where YBCO replaces the coils. It was considered a singular configuration efficiency with $\eta = 91\%$.

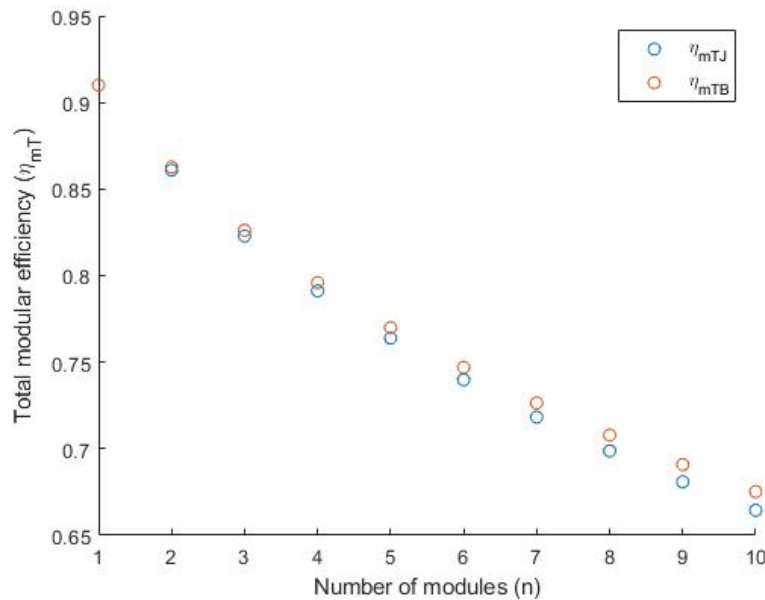


Figure 4.8: Modular efficiency in function of number of modules

It is possible to conclude that with the increase of modules, the efficiency of a machine with YBCO as coils starts to decreases when compared with another with YBCO as PM.

4.2.3 Machine with YBCO as coils

In a machine with YBCO instead of copper coils, the equation 2.22 becomes

$$P_T = P_{iron} + P_{HYBCO} \quad (4.23)$$

Considering the analytic relation found in (4.16), the equation 4.23 becomes the relation

$$P_T \propto 2l^3 + l^{1,173} \quad (4.24)$$

Finally to compute the efficiency is necessary divide (4.24) through the nominal power

$$\frac{P_T}{P_N} \propto \frac{2}{l} + l^{-2,83} \quad (4.25)$$

The relation for the efficiency of a machine with YBCO in function of linear dimension is given by (4.26).

$$\eta_\beta = \frac{1}{1 + K_1 \left(\frac{2}{l} + \frac{1}{l^{2,83}} \right)} \quad (4.26)$$

In figure 4.9 is represented the comparison between the efficiency of a conventional PM machine, a machine with YBCO as PM and a machine with YBCO as coils.

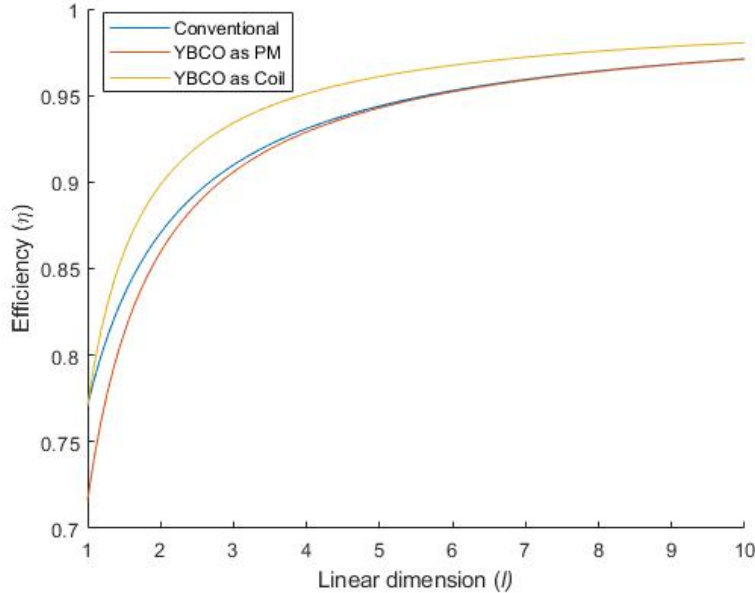


Figure 4.9: Efficiency of a conventional PM machine, a machine with YBCO as PM and a machine with YBCO as coils with increase of linear dimension.

It is possible to conclude that for smaller linear dimension values there is a difference, especially for YBCO as a coil. This happens because in this machine there aren't copper losses, enabling a higher value of efficiency. However, with the increase of linear dimension, the iron losses start to be the dominant factor, leading to a convergence in efficiency with the other machine designs.

Chapter 5

Experimental and FEM simulations

In this chapter, it was implemented different methods to validate experimentally the losses due to hysteresis founded through the analytic model. It was also created a simulated model in a FEM software for the same purpose.

5.1 Losses in YBCO - Experimentation

The purpose of this sub-chapter is experimentally computing the losses due to hysteresis in a YBCO bulk. Two different methods are purposed.

5.1.1 Experimental losses in a standard magnetic circuit

To understand how to compute experimentally the losses in a magnetic circuit is necessary to recap few concepts, starting with the simple magnetic circuit made of an iron core and one coil as shown in figure 5.1.

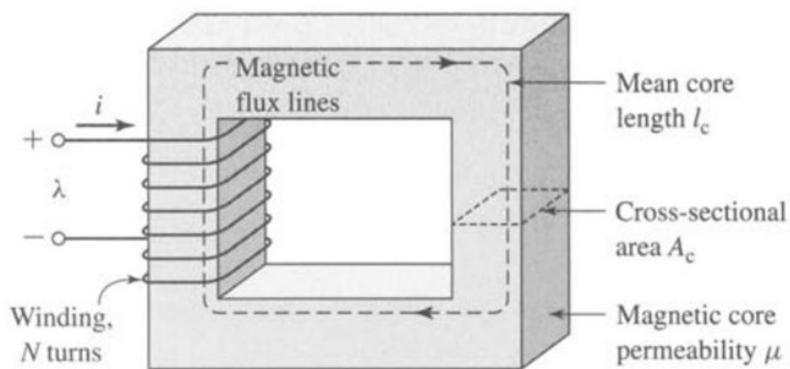


Figure 5.1: Simple Magnetic Circuit [13]

Some considerations need to be taken, the first one is that the core is composed by a magnetic material whose permeability, μ , is extremely bigger than the surrounding the material, air, μ_0 .

The cross-section is uniform and is excited by a winding with N turns, carrying a current of I . This current produces a magnetic field in the core, as shown in figure 5.1. Due to the high permeability, the magnetic flux is confined to the core and flow in the path represented in figure 5.1, also the flux density is uniform because the cross-sectional area is uniform [13].

The Maxwell equation (3.3) states that the net magnetic flux entering or leaving a closed surface is zero. This means that all the flux which enters the surface enclosing a volume must leave that volume over some other portion of that surface because magnetic flux lines form closed loops. This can be used to justify the assumption that the magnetic flux density (equation 2.6) is uniform across the cross-section of a magnetic circuit such as the core of figure 5.1 [13].

In this case, equation (2.6) is reduced to

$$\Phi = BA_c \quad (5.1)$$

Considering the integral form of equation (3.4) ,

$$\oint_C \mathbf{H} dl = \iint_S \mathbf{J} \cdot d\mathbf{a} \quad (5.2)$$

and that the source of the magnetic field in the core is the product Ni , known as magnetomotive force, F , equation (5.2) can be written as

$$F = Ni = \oint_C \mathbf{H} dl \quad (5.3)$$

The core dimensions are such that the path length of any flux line is close to the mean core length, l_c . As result, equation (5.3) becomes simply,

$$Ni = H_c l_c \quad (5.4)$$

where H_c is average magnitude of H in the core.

As can be seen through figure 5.2, the typical B(H) curve for a certain material, without considering hysteresis (anhysteretic), is composed by a linear zone and a non-linear zone. In the non-linear zone occurs the saturation, which represents the point from where the increasing of H does not imply the same increase of B in the material.

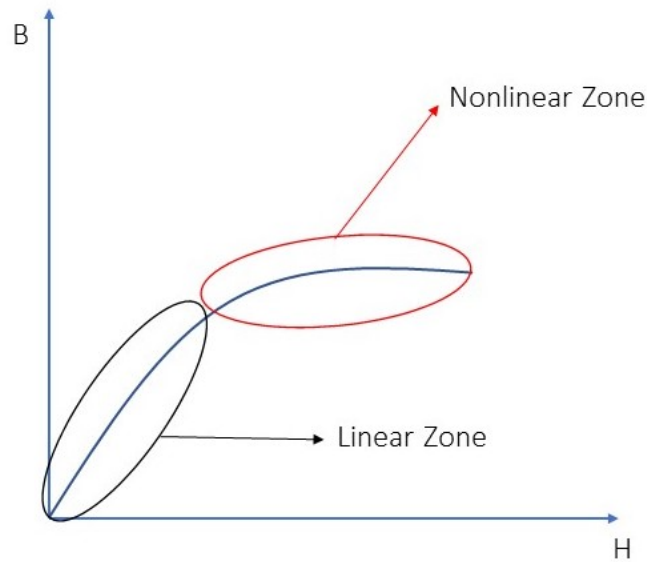


Figure 5.2: Typical B(H) anhysteretic curve

However, B and H cannot be measured directly, they need to be computed through equations (2.4) and (5.4), concluding that B is a function of voltage and H is a function of current.

When a sinusoidal voltage is put on the terminal's coil, the current waveform will be sinusoidal if the material stays in the linear zone. When the material reaches the non-linear zone, a small variation in voltage causes a major variation in the current leading to a current waveform with a triangular shape, as figure 5.3 shows.

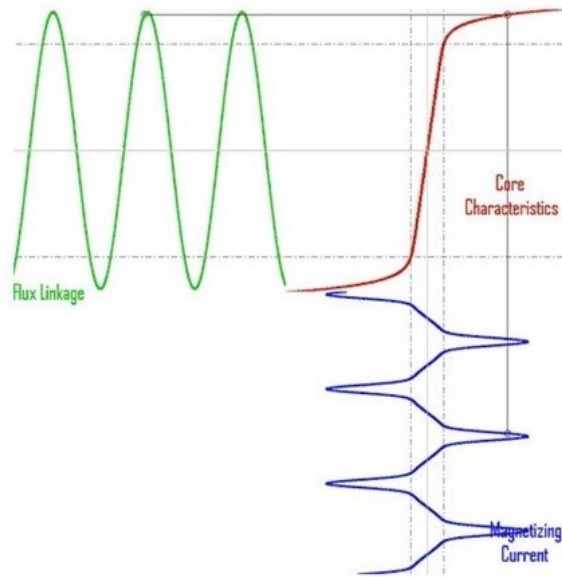
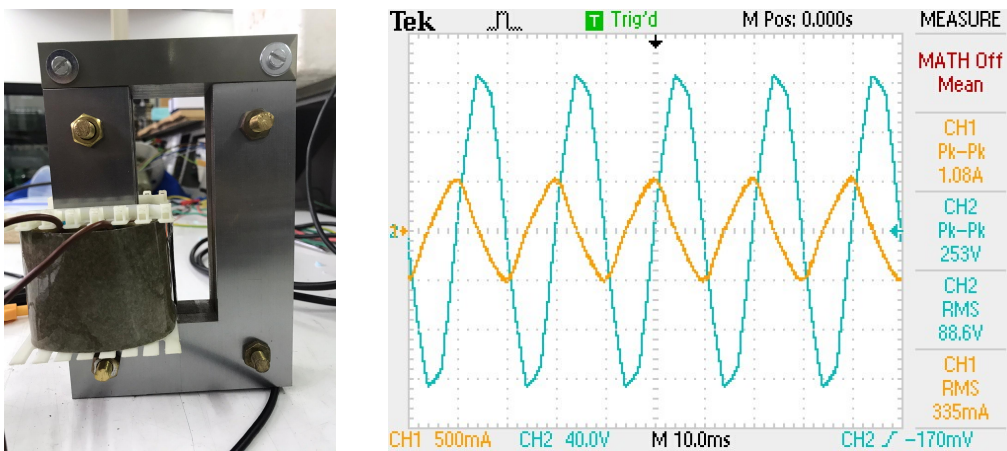


Figure 5.3: Example of Saturation Current [16]

Figure 5.4 shows an experimental example of current saturation. As it is possible to see, the current start to enter in the non-linear zone, becoming triangular. However, it is still far from the saturation zone because don't have the same shape as the current in figure 5.3.



(a) Experimental circuit

(b) Experimental current (yellow) and voltage (blue)

Figure 5.4: Experimental circuit and data

5.1.2 Experimental losses in a YBCO bulk as in a magnetic circuit

The first method used to find the hysteresis losses in YBCO was trying to discover the non-linear zone of this material through the current shape and after that compute the losses. For that, two coils of 400 turns were placed on top of each other, connect in series and the YBCO material placed in the middle as shown the illustration in 5.6. In figure 5.5 is shown the experimental setup used, without the liquid nitrogen necessary during the experiment to cooled the YBCO.

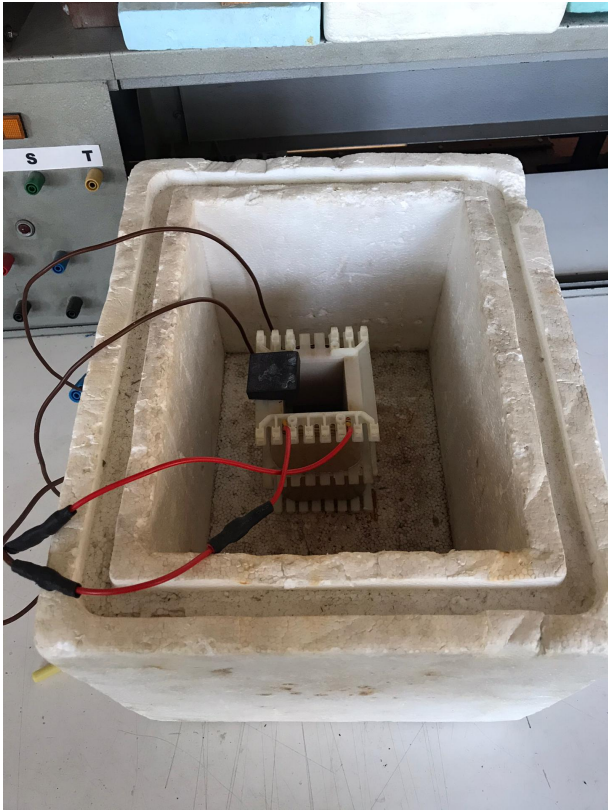


Figure 5.5: Experimental 2 coils of 400 turns each

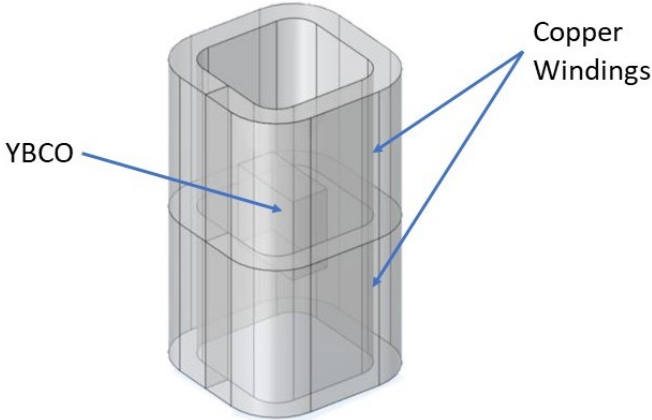


Figure 5.6: Illustration of experimental set up

Figure 5.7 represents the acquired voltage (at red) and current (at blue) from the experiment shown in figure 5.5.

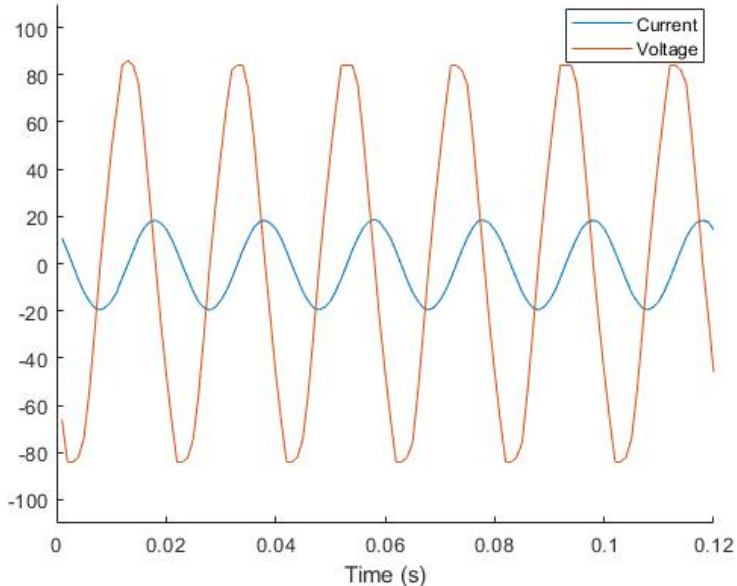


Figure 5.7: Experimental current (blue) in amperes and voltage (red) in volts YBCO bulk as in a magnetic circuit

Figure 5.8 represents the respective applied magnetic field.

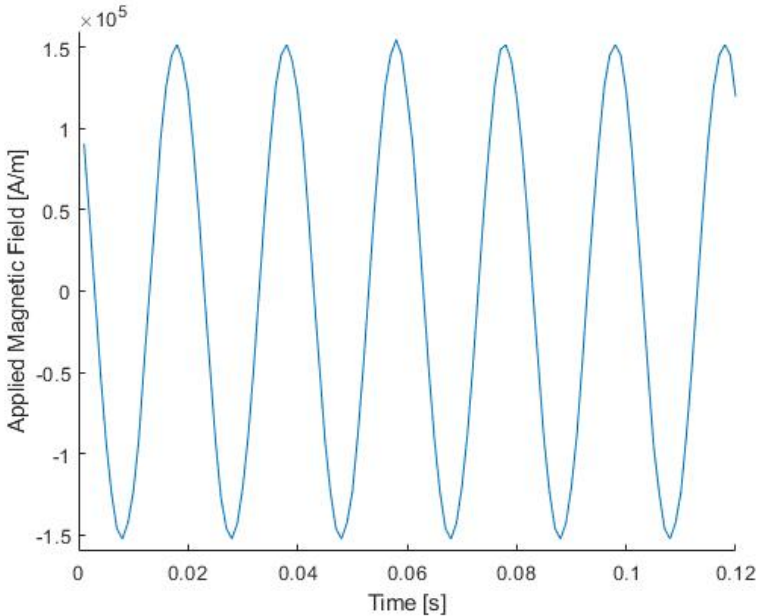


Figure 5.8: Experimental applied magnetic field for YBCO bulk as in a magnetic circuit

The first conclusion that can be taken is that neither the saturation nor the non-linear zone were reached because the current waveform is sinusoidal and not triangular. This means that the B-H curve of the material is still in the linear zone and it is necessary a higher applied magnetic field to reach the non-linear zone.

For achieve that, and due to the fact that exists a linear relation between turns and applied magnetic field, a coil with 4000 turns was used.

Figure 5.9 shows the experimental setup used without the liquid nitrogen necessary during the experiment to cooled the YBCO and 5.10 is an illustration of the experience.



Figure 5.9: Experimental set up for coil with 4000 turns

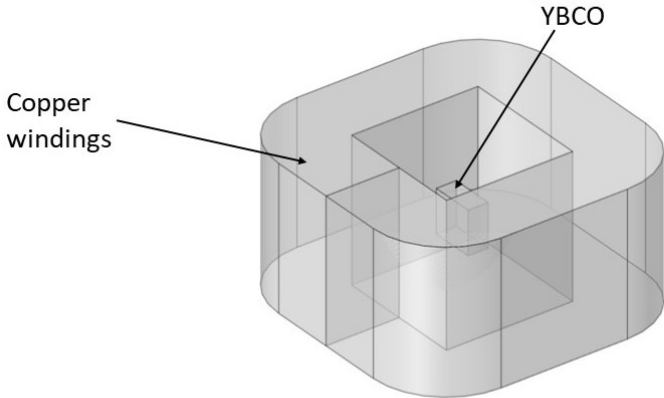


Figure 5.10: Illustration of experimental set up for coil with 4000 turns

Figure 5.11 shows the current and the voltage acquired experimentally.

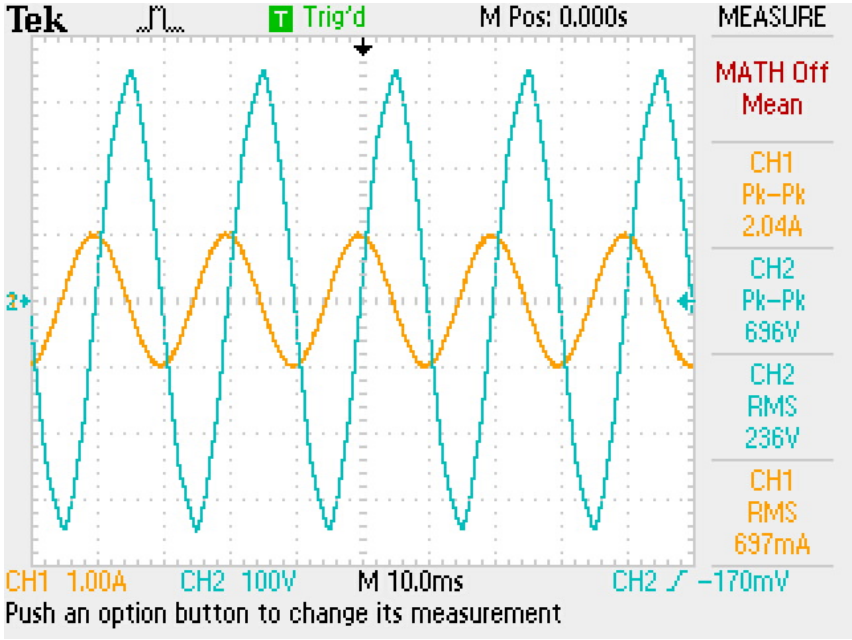


Figure 5.11: Experimental oscilloscope data

It is possible to conclude that when compared this solution with the previous one the number of turns in the copper winding increase from 800 to 4000 however, the maximum amplitude current reduces from 20A to 1A, and since this two variables changes linearly the applied magnetic field, the second scenario will have must lower applied magnetic field. With this conclusion, it was necessary to change the approach to calculate the losses.

5.1.3 Iron Core Solution

In this subsection, it will be present a solution for estimation of YBCO losses through the utilization of an iron core magnetic circuit.

The idea was using two different magnetic circuits, one with an air-gap and the other with the YBCO in the space of the air-gap, as present in figures 5.12 and 5.13, and compared the losses in both circuits.



Figure 5.12: Experimental magnetic iron core circuit

The total power in the magnetic circuit of the figure 5.12 is

$$P_T = P_{Cu} + P_{iron} \quad (5.5)$$

where P_{Cu} are the joule losses in the copper windings and P_{iron} are the iron losses, that are mostly composed by hysteresis losses due to the fact that the core is laminate.



Figure 5.13: Experimental magnetic iron core circuit with YBCO

The total power in the magnetic circuit of the figure 5.13 is

$$P_T = P_{Cu} + P_{iron} + P_{YBCO} \quad (5.6)$$

Assuming that the losses in the iron are the same (for the same current and voltage) in the two circuits, the only variable to find will be the losses in the YBCO.

In the table 5.1 are presented the power and respective losses at ambient temperature for the configuration illustrated in figure 5.12. To measured these values was used a Fluke 1735 Three-Phase Power Quality Logger.

Table 5.1: Power and losses at air temperature for circuit iron + coil with air-gap

P_T [W]	P_{Cu} [W]	P_{iron} [W]
9	5.19	3.81
35	20.2	14.8
75	42.77	32.23
125	68.95	56.05

With table 5.1 is possible to compute the power factor of the circuit and this value will be considered the same for the cooled magnetic circuit with YBCO and without. The coil resistance was measured in temperature ambient and cooled, having 1.5Ω and 0.3Ω , respectively.

The first measurement in a cooled environment was without YBCO and the results are shown in table 5.2.

In the second measurement was introduced the YBCO in the air-gap position, as illustrated in figure 5.13. It was considered that the iron losses remain the same. With these conditions, it was possible to compute the losses regarding to YBCO, as shown in table 5.3

Table 5.2: Power and losses for cooled circuit iron + coil with air-gap

P_T [W]	P_{cu} [W]	P_{iron} [W]
167.65	20.92	146.73

Table 5.3: Power and losses for cooled circuit iron + coil+ YBCO

P_T [W]	P_{cu} [W]	P_{iron} [W]	P_{YBCO} [W]
173.28	22.34	146.73	4.21

Considering that YBCO bulk as a volume of $13.5cm^3$, the power density losses in YBCO are $3.1 \times 10^5 W/m^3$.

When compared with the analytic value for the same applied magnetic field, there is a considerable difference since the analytic value is $4.3 \times 10^4 W/m^3$. This can happen due to multiple factors, one of them can be associated with the lack of accuracy in the measurement due to the chosen set up or the measurement instruments, the second factor can be related with some considerations made to compute the YBCO losses, like iron losses or power factor constant values, and the last factor can be related with the value founded through the analytic model since this model isn't extremely accurate for low magnetic field values.

To reach more precise values, it was developed a model through a FEM software.

5.2 FEM Model - Introduction

Based on sub-chapter 5.1, there are several potential errors in the experimental measurement that can lead to experimental results different from the results computed with the analytical model. To reduce these potential errors, an analysis through FEM software was considered.

For that, it was necessary to create two different geometries, completely equals in dimensions and shape to the ones used in the experimental setup. The first will be composed by an iron core and a coil and will be used to model the behaviour of the B-H curve in the iron core. In figure 5.14 is represented the design of this circuit. The other geometry will be composed by a coil, an iron core and a YBCO. Through the last geometry, it will be estimate the losses in YBCO in the same way as in the experimental part. Figure 5.15 represent the conceptual design of this circuit.

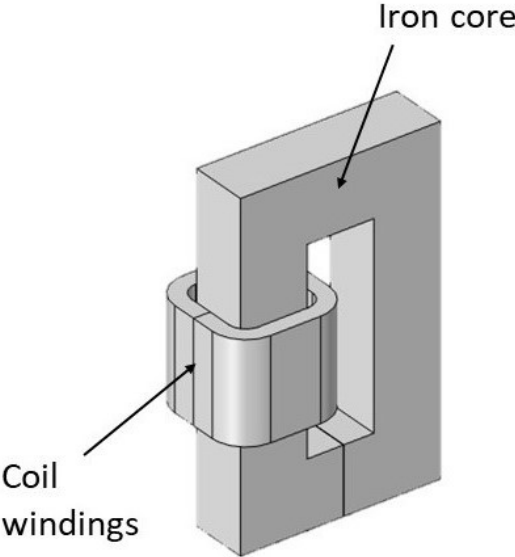


Figure 5.14: Conceptual design of circuit iron + coil

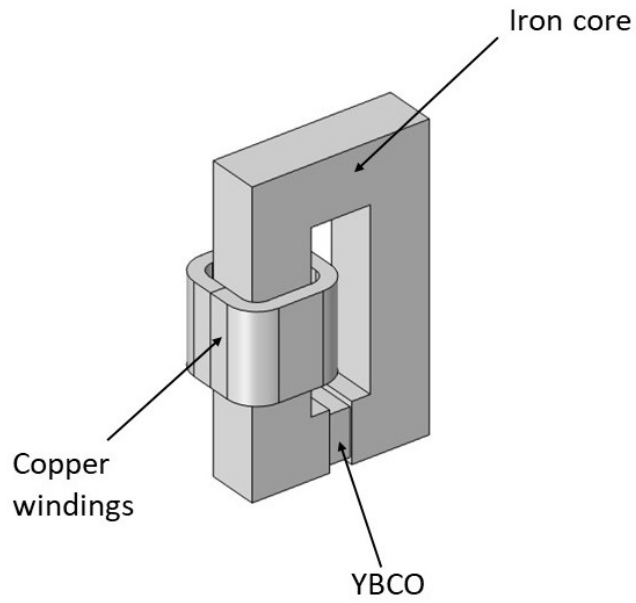


Figure 5.15: Conceptual design of circuit iron + coil +YBCO

5.3 FEM - Geometric Description of the System

5.3.1 Iron Core and Coil

Figure 5.16 shows the front view of the magnetic circuit. All measurements are in millimeters.

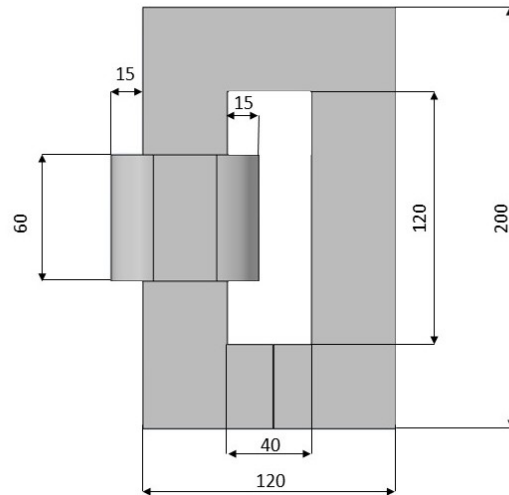


Figure 5.16: Front view of system iron + coil

Figure 5.17 shows the top view of the magnetic circuit. All measurements are in millimeters.

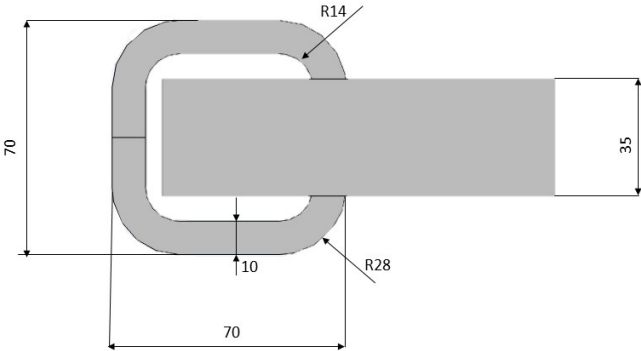


Figure 5.17: Top view of system iron + coil

5.3.2 Iron Core, Coil and YBCO

Figure 5.18 shows the front view of the magnetic circuit. All measurements are in millimeters.

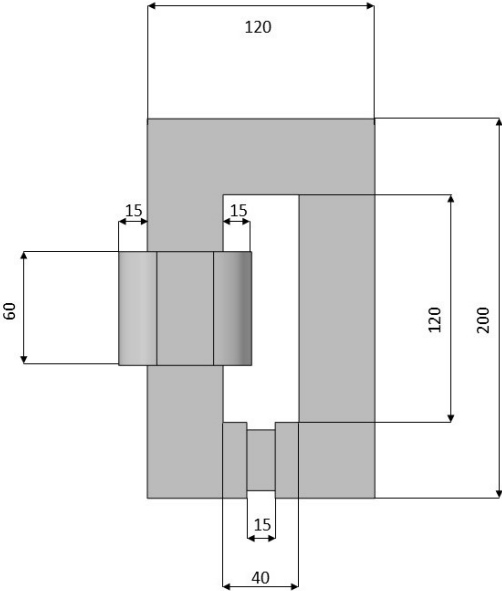


Figure 5.18: Front view of system iron + coil + YBCO

Figure 5.19(a) shows the YBCO front view and 5.19(b) shows the side view. All measurements are in millimeters.

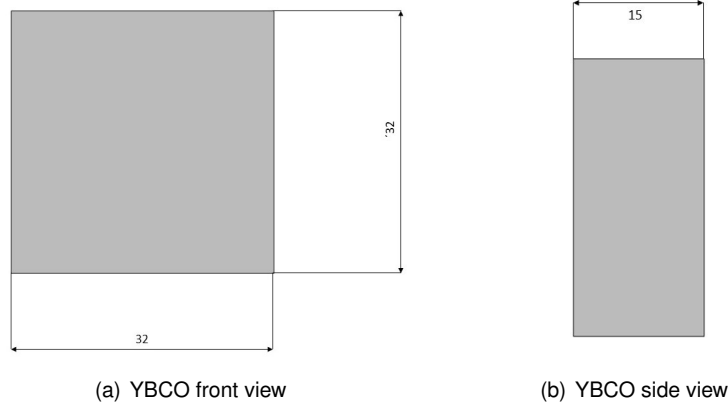


Figure 5.19: YBCO

5.4 FEM - Electromagnetic Model

5.4.1 A Formulation

This model assumed the \mathbf{A} -formulation. The variable \mathbf{A} is the magnetic potential vector and is defined through (5.7)

$$\nabla \times \mathbf{A} = \mathbf{B} \quad (5.7)$$

Through (3.2) and (5.7) it is possible to define the electric field vector as

$$\mathbf{E} = -\frac{\partial \mathbf{A}}{\partial t} \quad (5.8)$$

Considering that the current density vector can be defined in

$$\mathbf{J}_t = \mathbf{J}_e + \mathbf{J}_i \quad (5.9)$$

where \mathbf{J}_e is the external component and \mathbf{J}_i the internal component.

Considering the constitutive law in (3.6) and (5.8), the \mathbf{J}_i can be defined through (5.10)

$$\mathbf{J}_i = \sigma \mathbf{E}_i = -\sigma \frac{\partial \mathbf{A}}{\partial t} \quad (5.10)$$

Considering (3.4), the (5.10) can be defined as (5.11)

$$\nabla \times \mathbf{H} = \mathbf{J}_e - \sigma \frac{\partial \mathbf{A}}{\partial t} \quad (5.11)$$

Applying the vector operation *rot* in (5.8) at both sides of the equation and considering the constitutive law (3.5), the (5.11) can be defined as

$$\mu \nabla \times (\nabla \times \mathbf{A}) + \sigma \frac{\partial \mathbf{A}}{\partial t} = \mathbf{J}_e \quad (5.12)$$

and considering properties of the operator it is possible to achieve (5.14) that defines the **A**-formulation used in the FEM software.

$$\mu \nabla^2 \mathbf{A} + \sigma \frac{\partial \mathbf{A}}{\partial t} = \mathbf{J}_e \quad (5.13)$$

To define the HTS it is considered the constitutive law

$$\mathbf{J} = \sigma_{YBCO} \mathbf{E} \quad (5.14)$$

where σ_{YBCO} is the inverse of (3.15).

The iron material will be defined through (5.15)

$$\mathbf{B} = f(\mathbf{H}) \quad (5.15)$$

where function $f(\mathbf{H})$ is defined through the Jiles-Atherton model.

5.4.2 Jiles Atherton Model

The Jiles-Atherton model [17] is a model that defines the curve B-H of a material with hysteresis through an analytic model, this will be the model used to define the B-H curve for the iron core. For that, the model finds the magnetization derivative in function of the applied magnetic field, known as susceptibility, χ , through the following equations,

$$H_e = H + \alpha M \quad (5.16)$$

$$M_{an} = M_s \left(\coth \frac{H_e}{a} - \frac{a}{H_e} \right) \quad (5.17)$$

$$\frac{dM_{an}}{dH_e} = \frac{M_s}{a} \left[1 - \left(\coth \frac{H_e}{a} \right)^2 + \left(\frac{a}{H_e} \right)^2 \right] \quad (5.18)$$

$$\frac{dM_{irr}}{dH} = \frac{M_{an} - M}{k\delta(1-c) - \alpha(M_{an} - M)} \quad (5.19)$$

$$\chi = \frac{dM}{dH} = \left[c \frac{dM_{an}}{dH_e} + (1-c) \frac{dM_{irr}}{dH} \right] \frac{1}{1-ac} \quad (5.20)$$

where H is the applied magnetic field, M is the magnetization, M_s is the magnetization saturation, M_{an} is the anhysteretic magnetization, M_{irr} is the irreversible magnetization, δ is a parameter that depend on the signal of $\frac{dH}{dt}$ and α, a, c and k are the unknown parameters that change the shape of the B-H curve, for different materials. To find this parameters that generates the B-H curve that better fits the experimental one, the algorithm in [18] and the Matlab/Simulink non linear inductor were used.

In table 5.4 are shown the Jiles-Atherton parameters that better fit the experimental iron core.

Table 5.4: Jiles-Atherton iron parameters

Parameters	
M_S	$1.1827 \times 10^6 [A/m]$
a	$61.86 [A/m]$
k	$900 [A/m]$
c	0.04
α	2×10^{-4}

In figure 5.20 are represent two B-H curves for the iron core, in blue the experimental one acquired in laboratory and in red the simulation through Jiles-Atherton parameters shown in table 5.4. In terms of hysteresis losses, this two curves have a difference of 0.6%.

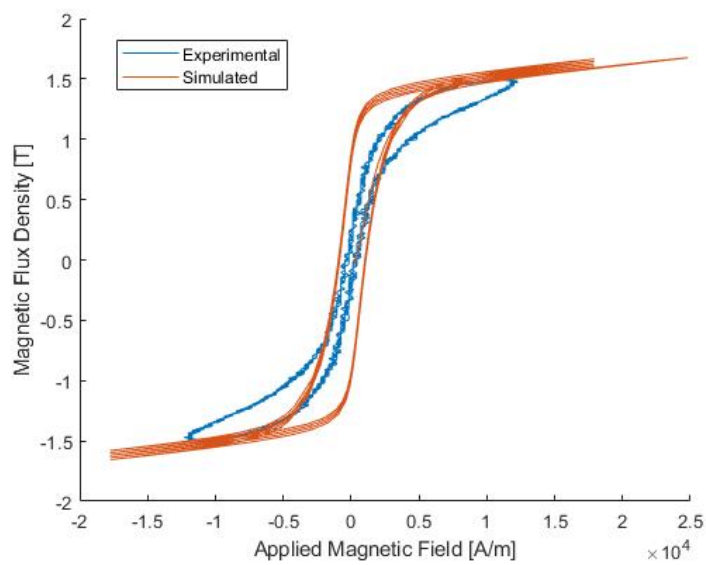


Figure 5.20: Experimental and simulated B(H) curves

It is possible to conclude that the simulated curve is a valid approximation of the experimental one since the hysteresis losses and the saturation values are quite the same. Adding to this, the simulated curve has a more standard shape, this not happen in the experimental one due to the degradation of the materials used or due to errors in measurements.

5.5 FEM - 3D Model for Iron and Coil

The 3D model used will be the one represented in figure 5.14 surrounding by air. It will be a time dependent simulation, where the magnetic field is generated through the coil, assuming a A-formulation. The B-H curve for the iron core is defined through the Jiles-Atherton model using the parameters in table 5.4.

5.5.1 3D Simulation

A voltage of 300V at 50Hz was applied in the coil and it was considered a 0.02s simulation to eliminate all the transient components.

In figures 5.21 and 5.22 are represented simulations results considering the magnetic flux density.

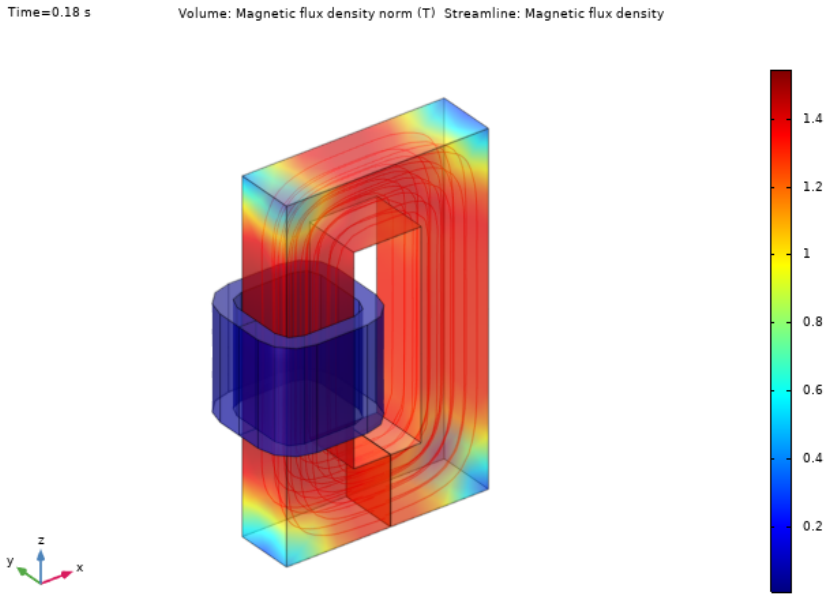


Figure 5.21: Magnetic flux density norm and streamlines results for an isometric view

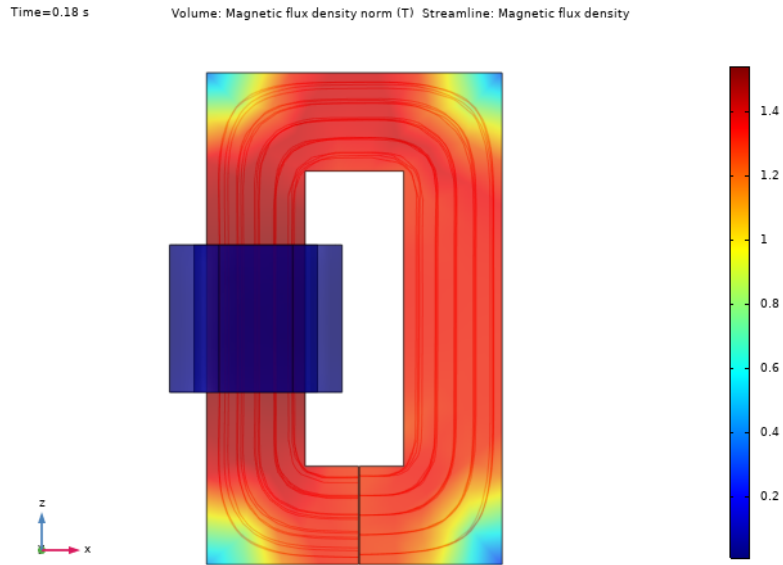


Figure 5.22: Magnetic flux density norm and streamlines results for a side view

In figure 5.23 are represented two B-H curves, at blue the experimental one and, at red the one generates through the FEM software simulation. These two curves have a difference in hysteresis losses of 12%. This difference was expected since the simulated curve in 5.20 was an ideal curve, however the FEM software considers aspects like dispersion, the non-uniformity of the magnetic field or the real path of the magnetic field instead of the mean path, and this can change the optimal Jiles-Atherton parameters.

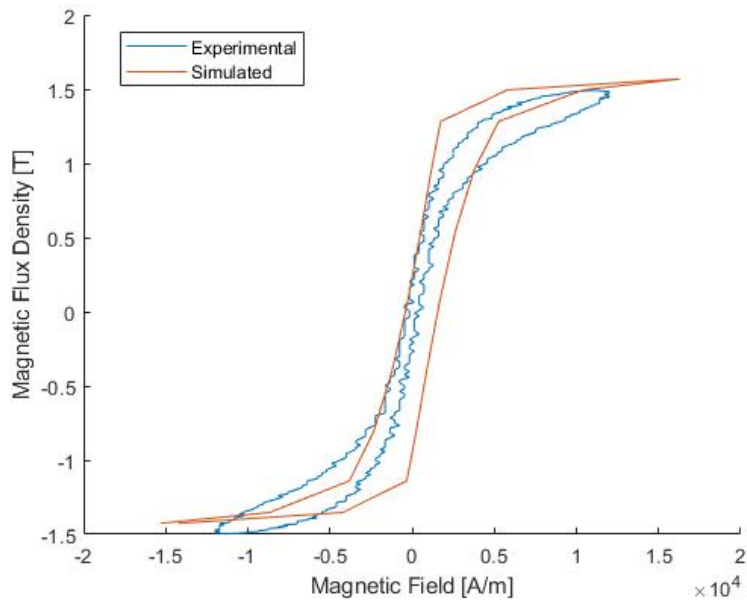


Figure 5.23: Experimental and simulated B(H) curve

In figure 5.24 is represented the current, at green, and the voltage, at blue, for the simulation.

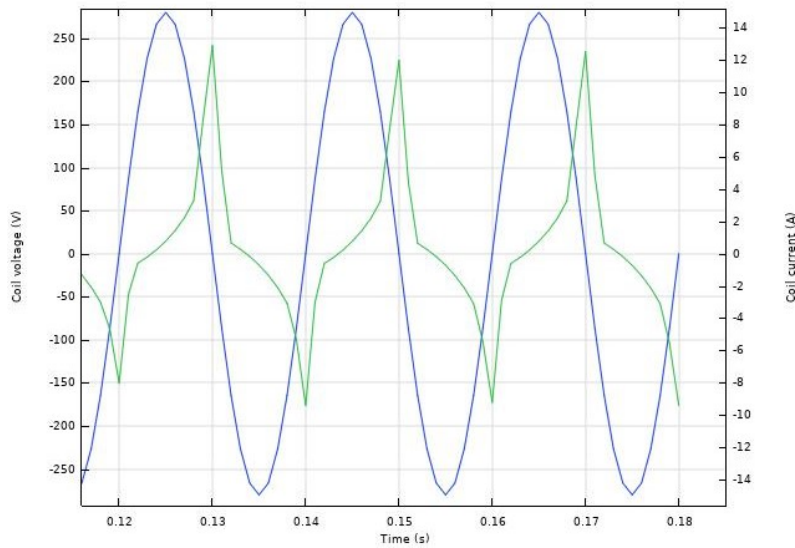


Figure 5.24: Current at green and voltage at blue compute through FEM software

In figure 5.25 is represented the current, at blue, and the voltage, at red, acquired experimentally for the same conditions as the simulation.

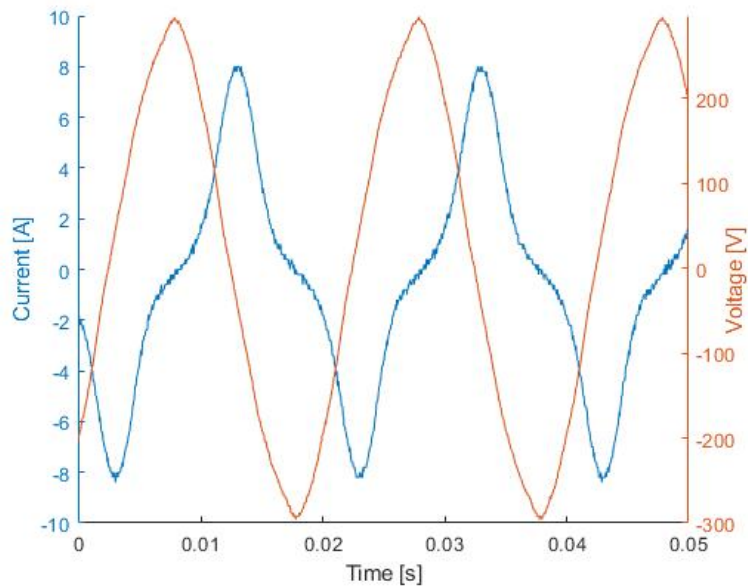


Figure 5.25: Current and voltage acquired experimentally

It is possible to conclude that the shape of the current is identical, this indicates that the simulated model can model the saturation in the iron core. However, the maximum values are different, this was expected due to the differences observed in 5.23.

5.5.2 Power losses

Considering that the active power in the circuit iron + coil is given through equation (5.21)

$$P = U_{RMS} I_{RMS} \cos(\phi) \quad (5.21)$$

where ϕ is the phase angle between current and voltage. The phase angle can be compute using the equation (5.22)

$$\phi = \tan^{-1} \left(\frac{X_L}{R} \right) \quad (5.22)$$

where R is the DC resistance and X_L the reactance associated to the magnetic circuit.

In table 5.5 are represented the computed values for this simulation

Table 5.5: RMS voltage and current and power factor for simulated model iron + coil

U_{RMS} [V]	I_{RMS} [A]	$\cos(\phi)$
197.98	4.84	0.032

Considering (5.5), it is possible to compute the losses due to iron. Table 5.6 represent the total power and respective losses.

Table 5.6: Power and losses for simulated model iron + coil

P_T [W]	P_{cu} [W]	P_{iron} [W]
30.65	19.89	10.76

5.6 FEM - 3D Model for Iron, Coil and YBCO

The 3D model used will be the one represented in figure 5.15 surrounding by air. It will be a time dependent simulation, where the magnetic field is generated through the coil, assuming a A-formulation. The B-H curve for the iron core is defined through the Jiles-Atherton model using the parameters in table 5.4 and the YBCO is defined through (5.14).

5.6.1 3D Simulation

A voltage of 300V at 50Hz was applied in the coil and it was considered a 0.02s simulation to eliminate all the transient components.

In figure 5.26 is represented the simulation result considering the magnetic flux density.

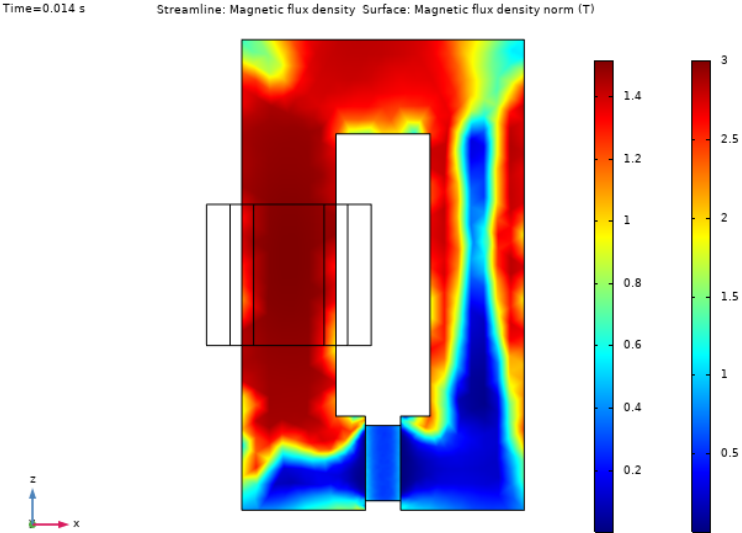


Figure 5.26: Magnetic flux density norm results for a side view for a Iron, Coil and YBCO system

In figure 5.27 is represented the current, at blue, and the voltage, at green, for the simulation.

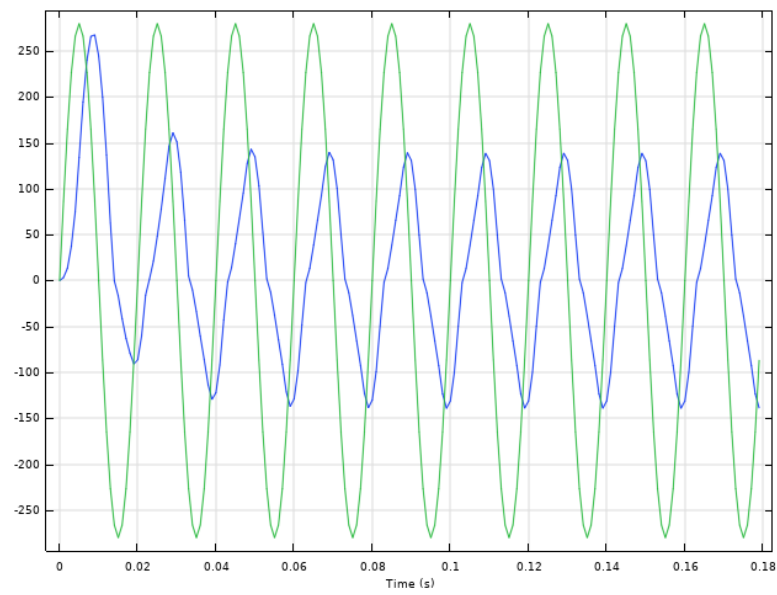


Figure 5.27: Current, at blue, and voltage, at green, compute through FEM software for a Iron, Coil and YBCO system

As it possible to see, the values of current and the shape of current aren't any similar between 5.27 and 5.25, this invalidates any possible iron losses computation.

Chapter 6

Conclusions

6.1 Achievements

This dissertation is divided in two parts: the first one related with the application of scale laws, using the KIM analytical model for HTS; and the second part is the experimental tests and FEM simulations.

Regarding the scale laws, the KIM model was implemented to study the losses due to hysteresis in HTS. With the results of those studies, and based on those scale laws, it was possible to develop scale relations for the HTS, i.e., the relationship between the hysteresis losses with its volume, current density and magnetic flux density. These relations allowed a comparison between conventional PM machines and new superconducting machines, where the HTS can either replace the PM or the coils. It was found by scale laws that HTS electric machines are indicative of having higher efficiencies and more power dense, however, the machine's topologies need to be different, especially using HTS as permanent magnets.

The experimentations were inconclusive, not being precise enough to quantify with good measure the hysteresis losses of the YBCO bulks. the FEM simulations also did not prove to be useful, since they did not validate the experimental tests

6.2 Future Work

To guarantee a more broad spectrum of results, other types of electrical machines need to consider. Considering another type of electrical machine implies changing some relations of the scale laws, especially in considering if the current densities or the magnetic flux density remain constant, or if they have a dependency between one another.

Regarding the experimental part, the simulations need to be made in a more controllable environment, with more precision in the measurements, coupled with a consistent FEM model of the experimentations, to validate the results of the KIM model, and consequently, the scale laws.

Bibliography

- [1] Jacek F Gieras, Fellow, IEEE. *Superconducting Electrical Machines State of the Art*. Przegląd Elektrotechniczny, December 2009.
- [2] A. Leão Rodrigues. *New Electric Reluctance Motor with Bulk Superconducting Materials on the Rotor*. Kusadasi, June 2001.
- [3] João Arnaud. *Use of superconductors in the excitation system of electric generators adapted to renewable energy sources*. Master's thesis, Instituto Superior Tecnico, Universidade de Lisboa, 2015.
- [4] Mircea Popescu, Stjepan Stipetic and Damir Zarko. *Scaling Laws for Synchronous Permanent Magnet Machines*. 2015 Tenth International Conference on Ecological Vehicles and Renewable Energies (EVER).
- [5] João Fernandes. *Gerador Eólico Polifásico de Fluxo Transverso com Magnetos Permanentes*. Master's thesis, Instituto Superior Tecnico, Universidade de Lisboa, 2011.
- [6] Pedro Lobato. *Paradigmas Construtivos da Máquina Elétrica de Relutância Comutada*. PhD thesis, Faculdade de Ciências e Tecnologia, Universidade Nova de Lisboa, 2015.
- [7] Francisco Silva. *ZFC Superconductor Magnetic Levitation System "Maglev-Tuga"*. Master's thesis, Instituto Superior Técnico, Universidade de Lisboa, 2018.
- [8] J. Bardeen, L. N. Cooper and J. R. Schrieffer. *Theory of Superconductivity*. Department of Physics, University of Illinois, Volume 108, number 5 December 1, 1957.
- [9] Angelina Orthacker. *Superconductivity*. Graz University of Technology, Graz (TU Graz).
- [10] Gren Ireson. *Discovering Superconductivity - An Investigative Approach*. Nottingham Trent University, Nottingham, UK, p.80-81, 2012.
- [11] Nicholas Brazier. *Superconductivity*. Phys 212X, April 24, 2017.
- [12] D.-X.Chen and R.B.Goldfarb. *Kim model for magnetization of type-II superconductors*. Journal of Applied Physics 66, 2489 (1989).
- [13] A. E. Fitzgerald, Charles Kingsley, Jr. and Stephen D. Umans. *Electric Machinery*. McGraw-Hill, New York, ISBN 0-07-112193-5, 1951.

- [14] António Costa. *Conception, study, optimization and prototyping of a horizontal axis HTS ZFC radial levitation bearing*. PhD thesis, Instituto Superior Técnico, Universidade de Lisboa, 2020.
- [15] José R. Simões Moreira. *CONDUÇÃO DE CALOR EM CILINDROS COM GERAÇÃO INTERNA DE CALOR e COEFICIENTE GLOBAL DE TRANSFERÊNCIA DE CALOR*. USP, Agosto 2016. <http://www.usp.br/sisea/>
- [16] Babak. K. Shandiz. *Saturation current*. CC BY-SA 3.0, <https://creativecommons.org/licenses/by-sa/3.0>
- [17] N.C. Pop and O.F. Caltun. *Jiles–Atherton Magnetic Hysteresis Parameters Identification*. “Al. I. Cuza” University, Faculty of Physics Carpath Center, 700506 Iasi, Romania, February 23, 2011.
- [18] N.C. Pop and O.F. Caltun. *ALGORITHM TO DESCRIBE MAGNETIZATION CURVES BY USING JILES ATHERTON MODEL*. “Al. I. Cuza” University, Faculty of Physics Carpath Center, 700506 Iasi, Romania, August 28, 2010.